

Consistent View of Polypeptide Chain Expansion in Chemical Denaturants from Multiple Experimental Methods

Alessandro Borgia,^{*,†,§} Wenwei Zheng,^{‡,§} Karin Buholzer,[†] Madeleine B. Borgia,[†] Anja Schüller,^{||} Hagen Hofmann,^{†,◇} Andrea Soranno,[†] Daniel Nettels,[†] Klaus Gast,^{*,||} Alexander Grishaev,^{*,⊥} Robert B. Best,^{*,‡} and Benjamin Schuler^{*,†,#}

^{††}Department of Biochemistry and [#]Department of Physics, University of Zurich, Winterthurerstrasse 190, 8057 Zurich, Switzerland

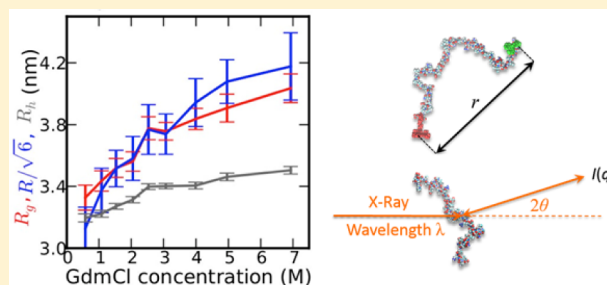
[‡]Laboratory of Chemical Physics, National Institute of Diabetes and Digestive and Kidney Diseases, National Institutes of Health, Bethesda, Maryland 20892-0520, United States

^{||}Physical Biochemistry, University of Potsdam, 14476 Potsdam, Germany

[⊥]National Institute of Standards and Technology and the Institute for Bioscience and Biotechnology Research, University of Maryland, Rockville, Maryland 20850, United States

Supporting Information

ABSTRACT: There has been a long-standing controversy regarding the effect of chemical denaturants on the dimensions of unfolded and intrinsically disordered proteins: A wide range of experimental techniques suggest that polypeptide chains expand with increasing denaturant concentration, but several studies using small-angle X-ray scattering (SAXS) have reported no such increase of the radius of gyration (R_g). This inconsistency challenges our current understanding of the mechanism of chemical denaturants, which are widely employed to investigate protein folding and stability. Here, we use a combination of single-molecule Förster resonance energy transfer (FRET), SAXS, dynamic light scattering (DLS), and two-focus fluorescence correlation spectroscopy (2f-FCS) to characterize the denaturant dependence of the unfolded state of the spectrin domain R17 and the intrinsically disordered protein ACTR in two different denaturants. Standard analysis of the primary data clearly indicates an expansion of the unfolded state with increasing denaturant concentration irrespective of the protein, denaturant, or experimental method used. This is the first case in which SAXS and FRET have yielded even qualitatively consistent results regarding expansion in denaturant when applied to the same proteins. To more directly illustrate this self-consistency, we used both SAXS and FRET data in a Bayesian procedure to refine structural ensembles representative of the observed unfolded state. This analysis demonstrates that both of these experimental probes are compatible with a common ensemble of protein configurations for each denaturant concentration. Furthermore, the resulting ensembles reproduce the trend of increasing hydrodynamic radius with denaturant concentration obtained by 2f-FCS and DLS. We were thus able to reconcile the results from all four experimental techniques quantitatively, to obtain a comprehensive structural picture of denaturant-induced unfolded state expansion, and to identify the most likely sources of earlier discrepancies.



INTRODUCTION

Understanding the properties of unfolded and disordered proteins is an important goal in biophysics. This is first because the unfolded state of globular proteins represents the starting point for protein folding, and its properties are closely connected to theories of folding.^{1–6} Second, for the large class of intrinsically disordered proteins (IDPs), which do not fold even under physiological conditions (at least in the absence of their binding partners),^{7,8} the physical properties of their disordered states should be intimately related to their function, as has been demonstrated in several cases.^{9,10} A number of powerful experimental techniques have emerged which can shed light on highly disordered conformations, including single-molecule Förster resonance energy transfer (FRET),^{11,12} nuclear magnetic resonance (NMR),¹³ small-angle X-ray (or

neutron) scattering (SAXS or SANS),¹⁴ dynamic light scattering (DLS),¹⁵ two-focus fluorescence correlation spectroscopy (2f-FCS),¹⁶ and photoinduced electron transfer (PET).¹⁷ Ideally then it should be possible to construct a self-consistent description of unfolded and disordered states based on information from these different experiments.

However, a discrepancy has emerged in the literature regarding the effect of chemical denaturants on the radius of gyration (R_g) of unfolded proteins. With some exceptions,^{18–20} several studies using SAXS and SANS experiments did not find a statistically significant change in unfolded state R_g over the experimentally accessible range of denaturant concentration for

Received: June 16, 2016

Published: September 1, 2016

two-state folding proteins^{20–24} and for an IDP.²⁵ For larger proteins, collapse upon denaturant dilution has been observed in time-resolved SAXS experiments, but in those cases the presence of stable folding intermediates modulating the observed R_g cannot be excluded.^{26–28} In contrast, FRET^{11,29–35} and contact-based quenching experiments^{34,36} show an increase in the average distance between labeled sites with denaturant, and NMR,²⁰ DLS,^{15,37} 1- and 2f-FCS,^{38–40} as well as analytical size exclusion chromatography studies⁴¹ provide evidence for an increase in hydrodynamic radius (R_h) with increasing denaturant concentration. Such an expansion would be consistent with improved solvation by the denaturant solution,^{33,42,43} currently understood to be the mechanism by which chemical denaturants destabilize folded proteins.³³ The increase in average distance observed by FRET is accompanied by an increase of the polymer scaling exponent for the unfolded state.⁴⁰ However, even the fractal dimension (the inverse of the scaling exponent) measured by SAXS has been reported to be denaturant independent for several IDPs or the unfolded state of two-state proteins,^{23,25} although a urea-dependent fractal dimension has been found for reduced RNase A.⁴⁴ Thus, while the analysis of each type of experiment appears internally consistent, the outcomes from SAXS and FRET experiments have led to qualitatively different conclusions. Indeed, for the single protein that has been investigated by both methods so far (protein L^{21,31,45}), very different results have been obtained from SAXS and FRET experiments. The discrepancy persisted in recent follow-up efforts on protein L, in which the experimental conditions in SAXS were matched to FRET,²³ as well as in a study on the effect of denaturant on the R_g of polyethylene glycol (PEG) monitored by SANS and FRET²² (as for proteins, both urea and guanidinium chloride are known to associate favorably to PEG⁴⁶). In contrast, changes in the R_g of unfolded proteins upon variation in pH or reduction of disulfide bridges have been unequivocally identified by SAXS, illustrating its fundamental suitability for identifying changes in unfolded state dimensions.^{47,48} Therefore, a reconciliation of the observations from SAXS and FRET in denaturant is still lacking. Clearly it is critical to resolve this issue, because it implies that at least one of the experiments is being incorrectly interpreted, with implications for their application to other problems related to unfolded and intrinsically disordered proteins. Furthermore, the absence of denatured-state expansion would contradict common theories for the mechanism of chemical denaturation^{33,49,50} and would overturn our understanding of this important process.

Here, we set out to understand the origin of this disagreement. To do so, we have chosen to systematically study two different proteins by a broad array of experimental and computational techniques using identical solution conditions and samples across the different types of experiment. As much as possible, the same protein constructs were used for all experiments, apart from the addition of donor and acceptor chromophores for FRET and a single dye for 2f-FCS. For the proteins, we selected a destabilized mutant of the spectrin R17 domain (R17 C66A/L90A or R17d) and the intrinsically disordered activator for thyroid hormone and retinoid receptors (ACTR).^{51,52} This choice was motivated by the desire to capture different sequence properties, since ACTR lacks a stable fold whereas R17 folds into a three-helix bundle, as well as a difference in size (by 39 residues, sequences in Table S1). Importantly, both proteins can be studied over a wide range of denaturant concentrations, because ACTR does not fold in the

absence of a binding partner,^{51–53} and R17d is completely unfolded even at low denaturant concentration (note, however, that the collapse behavior is not affected by the destabilizing amino acid exchange in R17d and is very similar to other spectrin domains⁵⁴). Therefore, there is no need to separate out a folded-state population, otherwise a major complication for ensemble-averaged experiments. Furthermore, previous work has shown ACTR to have only low helical content in water,^{51,55} and residual helical structure was not detected for unfolded R17.⁵⁶ Therefore, these proteins should also not have an unusual predisposition toward collapse in water due to secondary structure formation. Both proteins are highly soluble, so that potential aggregation problems occurring at relatively high protein concentrations required for SAXS and DLS are minimized. We study each protein in both of the most commonly used chemical denaturants, urea and guanidinium chloride (GdmCl).

We investigated the degree of unfolded-state expansion via four different experimental techniques that probe directly either intramolecular distances or hydrodynamic radii (Figure 1). In the first class are single-molecule FRET experiments, which probe distance distributions between individual pairs of residues, exploiting the Förster relation between the FRET efficiency and the distance between pairs of fluorophore-labeled residues⁵⁷ (Figure 1a). The resulting average intramolecular

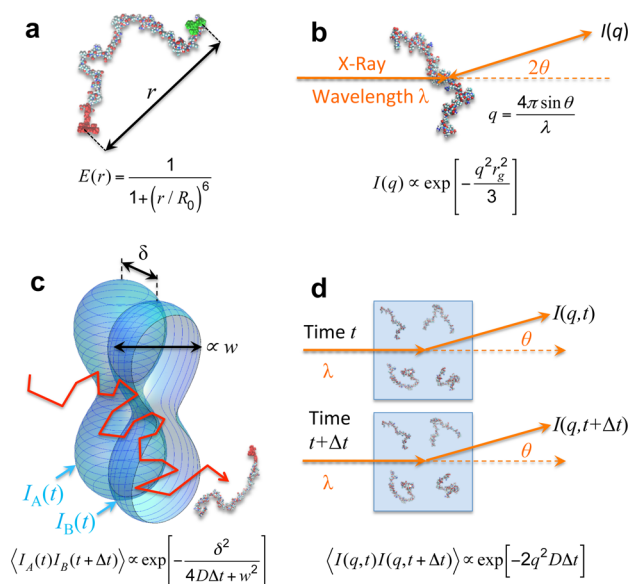


Figure 1. Schematic illustration of the different types of experiments used. (a) FRET efficiency, E , reports on the interchromophore distance, r ; R_0 is the Förster radius. (b) SAXS intensity, $I(q)$, is related to the radius of gyration, r_g , for small values of momentum transfer, q . (c) 2f-FCS measures the translational diffusion coefficient (D) from the fluorescence intensity cross-correlation of a molecule diffusing through two partially overlapping confocal laser foci separated by a distance δ and generated by orthogonally polarized pulsed interleaved beams of width w . (d) DLS measures D from the time correlation function of light scattering intensity fluctuations caused by changes of the mutual positions of molecules. Lower case r and r_g indicate the inter-dye distance and the radius of gyration of an individual conformation, respectively, as opposed to their capital counterparts signifying a value averaged over multiple conformations. Equations beneath figures are only meant to convey the important quantities evaluated in each technique and a general idea of how these observables are then used for data analysis.

distances and the R_g can then be estimated by using the statistics of a suitable polymer model.⁵⁸ The R_g can be obtained more directly from SAXS experiments by using a Guinier analysis of the scattering at very small angles from a monodisperse protein solution.⁵⁹ Provided the noise in the data is small enough, the linear region of the Guinier plot yields a model-free estimate of R_g (Figure 1b). Chain expansion can also be directly probed with SAXS by analyzing the fractal dimension at intermediate scattering angles.⁶⁰ Another quantity which is related to molecular size is the hydrodynamic radius, R_h , defined as the radius of a spherical object having the same translational diffusion coefficient, D , as the protein, according to the Stokes–Einstein relation. Although there is no simple quantitative relation between R_h and R_g for unfolded proteins, R_h is nevertheless expected to follow the same qualitative trend as R_g with increasing denaturant concentration. We used both 2f-FCS¹⁶ and DLS⁶¹ to obtain independent measures of R_h . 2f-FCS (Figure 1c) uses the correlations between photons from a labeled protein, recorded from overlapping detection volumes displaced by a fixed distance to measure D , and is thus less prone to instrumental artifacts (such as changes in the size of the observation volume with refractive index) than conventional single-focus FCS.¹⁶ Dynamic light scattering (Figure 1d) estimates D by analyzing the time correlation of light scattering intensity fluctuations due to the movement of the protein molecules in solution. D obtained by 2f-FCS and DLS can then be used to calculate R_h .

Thus, we have four independent measures of the effect of denaturant on unfolded state dimensions. For each type of experiment, we apply the standard analysis methods in order to extract the denaturant dependence of the average intramolecular distance (FRET), R_g (SAXS), or R_h (DLS and 2f-FCS). In addition, we integrated the SAXS and FRET data with molecular simulations via a Bayesian reweighting procedure,⁶² from which we infer representative ensembles of protein configurations that explain all of the experimental results. Each of the experimental techniques and the integrated analysis suggest that the chains expand with increasing denaturant concentration; moreover, the fitted ensembles are able to explain quantitatively both the FRET and the SAXS data as well as the two measures of R_h , indicating that all of the different types of experimental data can be interpreted consistently. Our results suggest a number of possible reasons for the apparent discrepancies reported previously. In particular, it is very challenging to observe expansion in equilibrium SAXS experiments due to (i) a smaller relative change in R_g than in the end-to-end distances probed by FRET, (ii) a large part of the expansion happening at low denaturant concentrations (inaccessible to ensemble-averaged measurements for stable folded proteins), and (iii) pronounced sensitivity of Guinier analysis to the range of scattering angles employed. Second, standard analysis of FRET experiments can slightly overestimate expansion.

RESULTS

Single-Molecule FRET. Förster resonance energy transfer probes the distance between a pair of residues labeled with chromophores via the well-known distance dependence of the transfer efficiency described by Förster theory.⁵⁷ Three different pairs of labeling positions were used both in ACTR and in R17d to map different segments of the chain (Table S1), and the six corresponding variants were measured in both GdmCl and urea. In Figure 2a and 2b, we show example FRET

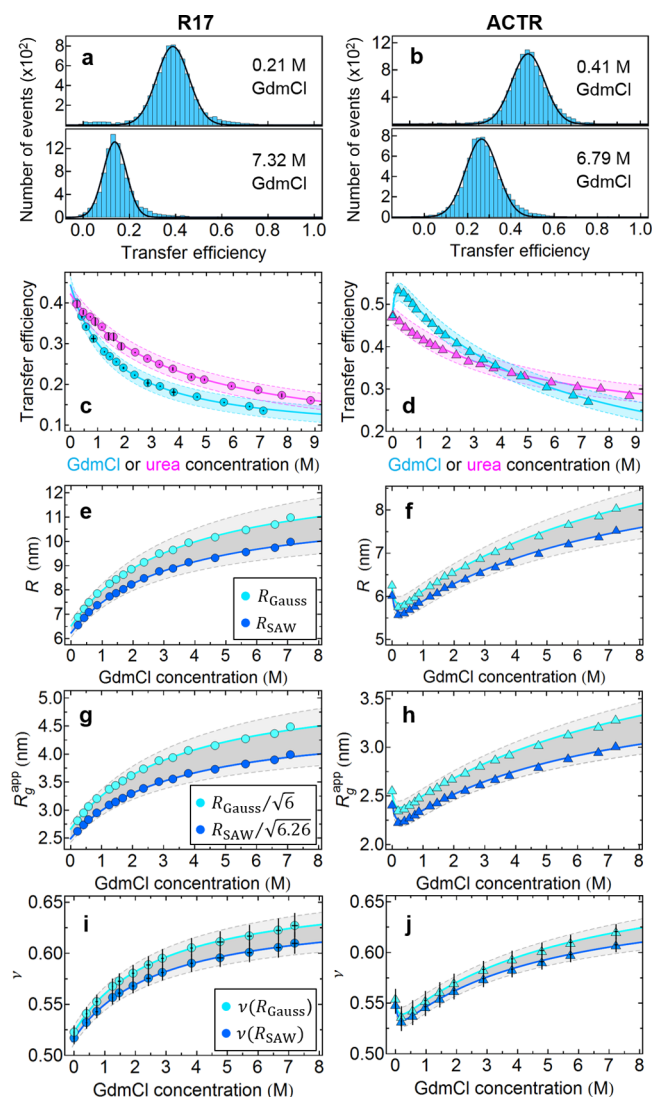


Figure 2. Single-molecule FRET analysis of R17d 1–116 (left column, circles) and ACTR 1–73 (right column, triangles) (Table S1). (a and b) FRET efficiency histograms at low and high denaturant concentrations. (c and d) Dependence of measured transfer efficiencies on GdmCl (cyan) and urea (magenta) concentration. Statistical errors from repeated measurements are reported as vertical and horizontal error bars; systematic errors in transfer efficiencies primarily due to instrument calibration (± 0.02) are indicated as shaded areas of the corresponding color. (e and f) Root-mean-square values of the end-to-end distance, R , as estimated by assuming the distance distributions of a Gaussian chain (cyan) or a self-avoiding walk (SAW, dark blue). Light shaded areas represent systematic errors propagated from those in transfer efficiency. (g and h) Apparent root-mean-square radii of gyration (R_g^{app}) as inferred from R (e and f), and the expected universal ratios for the Gaussian chain ($R^2/R_g^2 = 6$) or the SAW model ($R^2/R_g^2 \approx 6.26$), respectively.⁶⁸ Light gray shaded areas indicate the uncertainties from propagation of error (± 0.02) in transforming R^2 to R_g^2 . (i and j) Scaling exponents obtained by fitting the interdyde distances of the three different protein labeling variants (Table S1) simultaneously to $R = B|i - j|^{\nu}$ with a fixed B of 0.55 nm,⁴⁰ where i and j are the labeling positions of the respective variants for both the Gaussian and the SAW cases. Values and standard deviations from the fit are reported for the interdyde distances obtained assuming a Gaussian chain (cyan) and a SAW model (blue). Fits (solid lines) represent a weak binding model, including a polyampholyte contribution for ACTR in GdmCl.⁶³ Corresponding data in urea are shown in Figure S17.

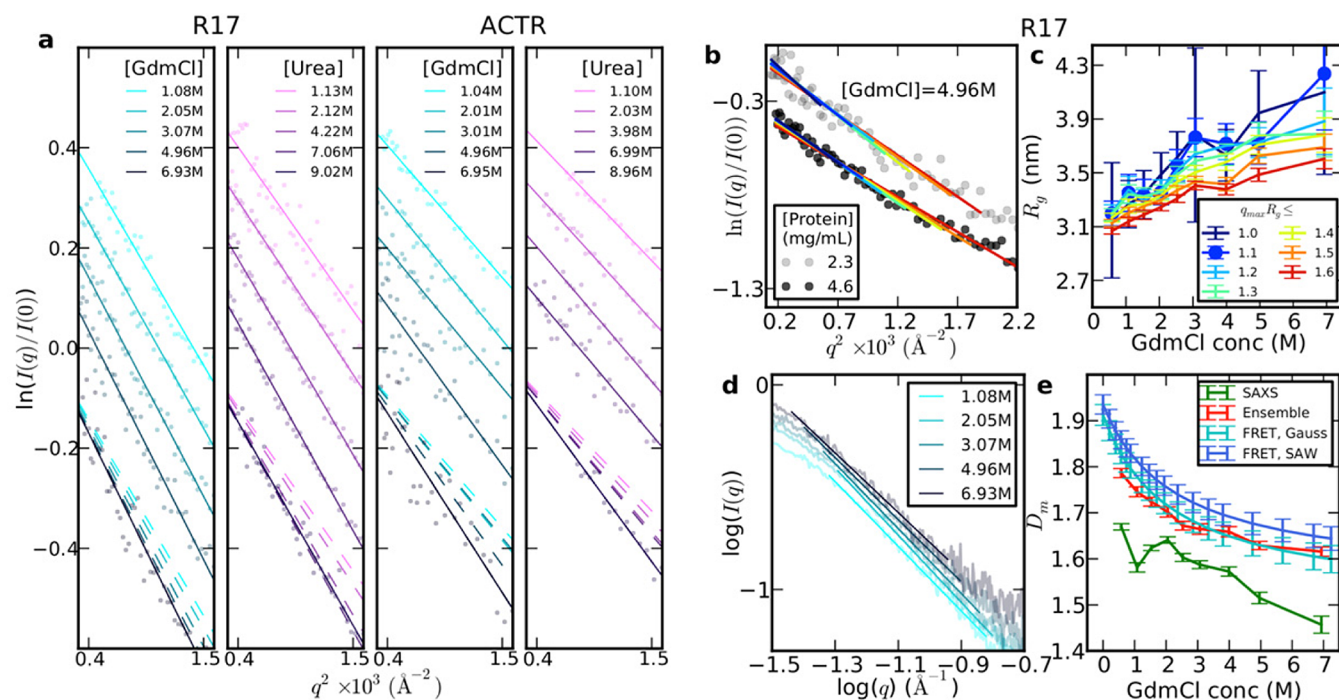


Figure 3. Small angle X-ray scattering (SAXS) data analysis of unfolded R17d and ACTR. (a) Guinier fits for R17d and ACTR in GdmCl and urea. Increasing denaturant concentrations colored from light to dark as indicated in the legend. For direct comparison, a copy of each fitted curve is also shown as a dashed line shifted down to the curve at the highest denaturant concentration. (b) Guinier fits within different ranges of $q_{\max}R_g$ for R17d in 4.96 M GdmCl as an example to show the underestimation of denaturant-induced expansion obtained using an increasing $q_{\max}R_g$ range, and (c) corresponding R_g for all GdmCl concentrations (see legend for color code of maximum $q_{\max}R_g$ in fitting). (d) Fitting mass fractal dimension, D_m , to the intermediate q range of R17d data in GdmCl (see legend for color code of GdmCl concentration), and (e) corresponding GdmCl-dependent D_m for R17d (data in the other protein-denaturant combinations are given in Figure S8). Mass fractal dimension from fitting SAXS intensity and from the inverse of the length scaling exponent from FRET with different polymer models (Figure 2i) and from reweighted structural ensembles are compared (see legend for color code).

efficiency histograms at low and high denaturant concentration (protein concentration ≈ 50 pM) for the N-/C-terminally labeled variants R17d-R1C/Q116C and ACTR S1C/S73C (“R17d 1–116” and “ACTR 1–73” in the rest of the paper), demonstrating the existence of a single (unfolded) population under all conditions, whose position shifts continuously with denaturant concentration (a larger set of histograms is shown in Figure S1). Equilibrium ensemble denaturation curves determined by intrinsic tryptophan fluorescence of R17d (unlabeled protein used for SAXS and DLS) confirm complete unfolding above ~ 0.2 M GdmCl (Figure S2). In Figure 2c and 2d we summarize the variation in mean transfer efficiency with denaturant concentration computed from FRET efficiency histograms for the four combinations of terminally labeled proteins and denaturants. Consistent results were obtained from the analysis of fluorescence lifetimes (Figure S3). In each case, there is a clear decrease in efficiency as the denaturant concentration is increased, indicating that the protein chain is expanding, a similar result to that obtained with other proteins.^{11,35,40,64} (For ACTR, an initial increase in transfer efficiency is observed at low concentrations of GdmCl because of screening of the electrostatic repulsion commonly observed in charged IDPs.^{58,63})

The FRET efficiency reports on the pair distance between the probe chromophores, but since a broad distribution of distances contributes to the observed signal, additional assumptions are needed to obtain quantitative distance information. (Additional aspects influencing the analysis, such as fluorescence lifetime and rotational averaging of the

fluorophores, are discussed in the SI.) The most commonly used analysis procedure assumes, as an approximation, the distance distribution, $P(r)$, of a suitable polymer model whose shape is determined by a single adjustable parameter, which is thus uniquely determined by the experimental transfer efficiency.^{30,31,35,58,65} From the resulting $P(r)$, a measure of the average interdye distance can be obtained, most commonly in terms of the root-mean-square distance, $R = \langle r^2 \rangle^{1/2}$. We used the $P(r)$ of several different polymer models to perform the conversion from transfer efficiency to R , namely, the Gaussian chain, the worm-like chain, the Sanchez model,^{31,33} and a self-avoiding walk (SAW), corresponding to a chain with excluded volume (details in SI text). The results illustrate some variability in the resulting R values due to the choice of $P(r)$, with the Gaussian chain and SAW yielding the largest and smallest values of R , respectively (Figure 2e and 2f), but all showing a clear swelling of the unfolded chain with increasing denaturant concentration, well outside the experimental error. On the basis of the analysis of molecular simulations including both excluded volume and attractive interactions, the $P(r)$ of a Gaussian chain provides reasonable values of R for relatively compact chains but tends to overestimate R for more expanded chains (Figure S4),^{58,65,66} leading to the largest apparent change in unfolded state expansion, while the SAW chain recapitulates the R from simulation remarkably well.

For a more direct comparison to SAXS data, an estimate of R_g can be made based on polymer theory that approximates the relation between R and R_g ($R_g = \langle r_g^2 \rangle^{1/2}$, where r_g is the radius of gyration of an individual conformation). Unfolded proteins

commonly explore a range of compactness between two limits: the Θ state, where attractive and repulsive chain–chain and chain–solvent interactions are balanced such that the polypeptide chain obeys the length scaling of an ideal chain,⁶⁷ and the excluded volume limit, typically approached at high denaturant concentration, where the chain interacts preferentially with the solvent and is dominated by repulsive intrachain interactions.⁴⁰ In this interval, R^2/R_g^2 is expected to vary between 6 and 6.26 for a Gaussian chain and a SAW, respectively,⁶⁸ the values that we use here for estimating bounds on R_g from FRET (Figure 2g and 2h, see SI text for details). Note that $\sim 50\%$ of the change in chain dimensions occurs below ~ 2.5 M GdmCl or ~ 3.5 M urea, with less variation over the higher concentrations, which are those commonly accessible in equilibrium ensemble-averaged experiments on folding-competent proteins. Although the observed increase in R_g of the unfolded ensemble is robust toward the choice of the particular polymer model, possible quantitative limitations of these simple models have been suggested earlier,^{63,65,66} prompting us to employ a Bayesian reweighting analysis based on ensembles of unfolded structures generated by molecular simulations to avoid these problems (see below).

An alternative measure of chain expansion is the scaling exponent, ν , which relates the average distance between points in the chain to their separation in sequence, N , via scaling laws of the form $R = B \cdot N^\nu$ (see also SI) and which can thus be estimated from the FRET-derived values of R . The value of ν is expected to be $1/3$ in poor solvent, i.e., conditions where the chain interacts strongly with itself and therefore is very compact (a regime not commonly explored by natural unfolded proteins), $\sim 1/2$ under Θ conditions (approximately corresponding to native buffer^{40,44}), and $\sim 3/5$ in good solvent (e.g., at high denaturant concentration^{40,69,70}).⁶⁷ Taking advantage of the observation that the prefactor, B , for proteins varies only within a narrow range,⁴⁰ we estimated the scaling exponent as a function of denaturant concentration from the analysis of the data for the three labeling variants of each protein in GdmCl and urea (see SI for details). Figure 2i and 2j shows the results, with a transition from values of ν close to $1/2$ at low, to values of $\sim 3/5$ at high denaturant concentrations, reflecting the expansion of the chain with increasing solvent quality.

SAXS. X-ray scattering from dilute, monodisperse protein solutions provides rich information on the distributions of interatomic distances within each molecule. We recorded solution X-ray scattering intensities, $I(q)$, for ACTR and R17d over a wide range of GdmCl and urea concentrations (between 0.32 and 6.95 M GdmCl and between 0.58 and 9.02 M urea). In addition, we recorded data at multiple protein concentrations ranging from ~ 4.6 to ~ 0.6 mg/mL (Figure S5) to check for the absence of artifacts due to intermolecular correlations and protein aggregation (further discussed in the DLS section below). We first apply the Guinier analysis as the most direct method to extract the radius of gyration from the data at small momentum transfer, q , where $I(q) \propto \exp[-q^2 R_g^2/3]$. Therefore, in the limit $q \rightarrow 0$, the slope of the Guinier plot of $\log[I(q)]$ versus q^2 should yield R_g directly. The Guinier plots for a representative set of denaturant concentrations are shown in Figure 3a for each protein and denaturant combination. Despite the apparent similarity of the full SAXS curves (Figure S5), we find a clear systematic variation of the slope in the Guinier region that indicates an increasing R_g with increasing denaturant concentration.

The Guinier approximation is valid only for a very limited range of $q \leq q_{\max}$, the accepted range for folded proteins being $q_{\max} R_g \leq 1.3$. However, this range is known to be more limited for unfolded proteins, since the higher order terms in the expansion from which the Guinier approximation is derived are larger for more extended conformations.^{44,71} Indeed, using increasing values of q_{\max} for Guinier fits leads to a systematic underestimation of R_g , as seen in Figure 3b, where we fitted the Guinier region for R17d in 4.96 M GdmCl using different values of $q_{\max} R_g$, clearly showing that the fitted radii of gyration become progressively smaller as $q_{\max} R_g$ increases. It is noteworthy that we observe a similar dependence of R_g on $q_{\max} R_g$ for lower protein concentrations, suggesting that this is not an artifact due to weak protein association (Figure 3b). To examine the influence of q_{\max} on the resulting expansion with increasing denaturant concentration, we also show in Figure 3c the estimated R_g as a function of GdmCl concentration for R17d using different limits for $q_{\max} R_g$. Employing larger $q_{\max} R_g$ limits to define the Guinier region results in a progressive suppression of the denaturant-induced increase in R_g . Similar results are obtained for other protein/denaturant combinations (Figure S6). However, as $q_{\max} R_g$ is decreased, the reduced number of data points available results in increasingly large errors, such that it becomes harder to detect a systematic change in R_g as $q_{\max} R_g$ is varied in the range 1.1–1.3 for R17d at any single denaturant concentration (Figure 3e). However, an inverse-variance weighted average of the ratio $R_g(q_{\max} R_g = 1.1)/R_g(q_{\max} R_g = 1.3)$ over all R17d data points in urea and GdmCl equals 1.018, and the corresponding value for $R_g(q_{\max} R_g = 1.0)/R_g(q_{\max} R_g = 1.1)$ equals 1.009. The trend is clearer for ACTR due to its smaller size and larger number of data points in a given $q_{\max} R_g$ range, resulting in higher precision for the fitted R_g values—the corresponding averaged ratios are 1.039 and 1.025. These observations indicate systematic differences in the R_g values determined throughout the entire commonly used $q_{\max} R_g$ range of 1.0–1.3 for both proteins studied here.

To complement the experimental analysis, we performed Guinier analysis on the scattering intensities calculated from all-atom MD simulations of ACTR,⁷² where scattering curves can be computed accurately down to much smaller angles than experimentally possible and which are free from concerns about sample imperfections (Figure S7) or data precision. In this case, we find that Guinier estimates of R_g achieve an accuracy better than 0.05 nm only for $q_{\max} R_g < 0.9$. Importantly, the value of this upper bound decreases with protein chain expansion, which could lead to larger suppression of an apparent fitted R_g relative to the true value at higher denaturant concentrations. This detrimental effect is further amplified by the removal of the experimental lowest- q data, which are inaccessible due to beam stop shadowing, stray scattering, and sample nonidealities, as well as by the decrease in the precision of these data due to a small number of detector pixels recording them and the increased capillary scattering, emphasizing the challenges of extracting the radius of gyration from the rather noisy experimental data at low angles. Finally, as observed with FRET, about half of all of the expansion occurs at the lower denaturant concentrations (below ~ 2.5 M GdmCl or ~ 3.5 M urea).

We can also obtain a direct estimate of the polymer scaling exponent, ν , from the SAXS intensities. At intermediate scattering angles above the Guinier range, the intensity has a power law dependence on q , i.e., $I(q) \propto q^{-D_m}$, where $D_m = 1/\nu$ is the mass fractal dimension. We estimate D_m by fitting the

linear region of a plot of $\log(I)$ against $\log(q)$ at intermediate q . Such fits are shown in Figure 3d for R17d in GdmCl (corresponding plots for R17d and ACTR in urea are given in Figure S8). It is important to note that while the linear region in this plot is expected to exist, its bounds may vary with the experimental conditions and become harder to select with confidence with the decreasing experimental signal/noise associated with the poorer contrast at high denaturant concentrations. We have chosen the linear region by minimizing χ^2 for a linear fit as a function of the position and width of the fitting window (details in Figure S8). Although the data at these q values are less precise than those within the Guinier range, we can nonetheless identify a systematic change in slope with denaturant concentration. The decrease in D_m obtained from SAXS, shown in Figure 3e, is qualitatively consistent with the increase of ν inferred from FRET and is similar to the decrease of D_m with increasing urea concentration previously observed for RNase A.⁴⁴

2f-FCS. To obtain an additional independent measure of protein expansion, we also quantified the hydrodynamic radius, R_h , of each protein as a function of denaturant concentration from its translational diffusion coefficient and the (independently measured) solvent viscosity using the Stokes–Einstein relation (details in SI text). 2f-FCS with a purely optical generation of two laterally displaced but overlapping foci (resulting in a fixed and well-defined distance) is a recently developed method for determining diffusion coefficients from fluorescently labeled molecules with high precision by measuring the correlation between photons detected in the two foci.¹⁶ It avoids some of the technical challenges of conventional (single-focus) FCS, such as optical saturation effects and changes in refractive index (a particularly important aspect for measurements at different denaturant concentrations). We measured R_h with 2f-FCS for R17d-Q116C singly labeled with a donor dye (R17d-488) and ACTR-S1C singly labeled with an acceptor dye (ACTR-594), both in GdmCl and urea, and find an increase in R_h with denaturant concentration in each case (Figure 4). However, the relative change in R_h over the accessible range of denaturant concentration is much smaller than for R and R_g , similar to previous observations of the coil-to-globule transition of homopolymers.⁷³

Dynamic Light Scattering. A second, independent, way of determining hydrodynamic radii is via DLS. In this case, the experiments were performed with unlabeled protein at concentrations of denaturant between 0.2 and 6.95 M GdmCl and between 0.58 and 9.02 M urea. The method uses the correlation times of scattering intensity fluctuations to determine molecular translational diffusion coefficients, and hence R_h ,⁶¹ and is sensitive to small variations in this parameter.⁷⁵ Effects from the nonideality of the solution due to the high protein concentrations required were investigated systematically by measurements at different protein concentrations (see SI text and Figure S9a,b). Again, we observe an increase in R_h with increasing denaturant concentration for all samples, very similar to that calculated from 2f-FCS (Figure 4). We note that although both DLS and 2f-FCS can measure R_h with high precision (corresponding to reliable relative changes in chain expansion), systematic errors (e.g., from determining the distance between the foci in 2f-FCS of about 2.5%) must be taken into account for the accuracy of the results (corresponding to the absolute values of R_h). Accordingly, both statistical and systematic errors are reported in Figure 4. Note also that the values from 2f-FCS are generally slightly larger than from

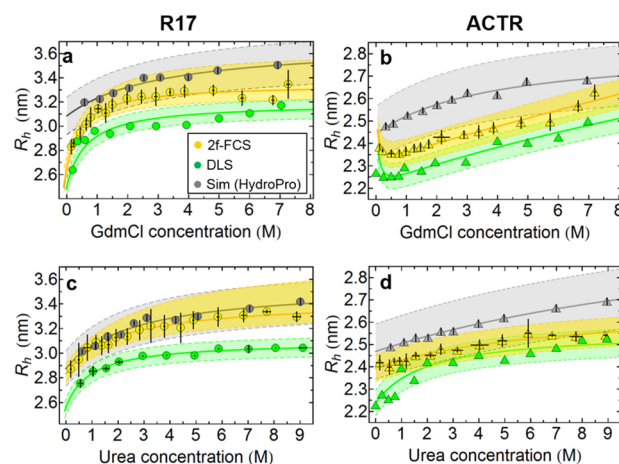


Figure 4. Denaturant dependence of the hydrodynamic radius (R_h) for R17d-488 (a and c) and ACTR-594 (b and d) in GdmCl and urea from 2f-FCS (yellow symbols) and for R17d and ACTR (both unlabeled) from DLS (green symbols). Also plotted is R_h calculated (using HydroPro⁷⁴) from the ABSINTH structure ensembles with weights determined from combined fits to the SAXS and FRET data (gray symbols). Values of R_h from 2f-FCS are the average of three or more independent measurements; error bars show the resulting standard deviations. Shaded areas indicate a 2.5% systematic error estimated for 2f-FCS and DLS measurements and a 5% average model error for the HydroPro calculation.⁷⁴ R_h values shown from DLS are either extrapolated to infinite protein dilution (d) or measured at the lowest possible protein concentration with sufficient signal-to-noise (see Figure S9a,b for plots of the protein concentration dependence of R_h in DLS experiments). Solid lines are fits to a weak binding model, including a polyampholyte contribution describing the initial collapse of ACTR at low GdmCl concentrations.⁶³

DLS, consistent with an increase in size due to the additional fluorophore attached to the protein for 2f-FCS. This result further suggests that the labeling with our fluorophores only increases the protein size slightly, while dye–protein interactions do not exert a detectable effect on the change in unfolded state expansion.

An additional benefit of using DLS is that it allowed us to quantify even small fractions of protein aggregates present in our samples in a range that would be difficult to detect by SAXS. Although R17 and ACTR are highly soluble proteins and we employed strict handling protocols to minimize aggregation (see SI text), we still found detectable traces of slow-diffusing particles in our samples (see SI text and Figure S9c,d): for both R17d and ACTR they amounted to less than 1% of weight concentration in all denaturant concentrations, and their presence was significantly reduced after centrifugation, which was part of the SAXS sample processing protocol before data acquisition (see SI). However, in order to estimate the magnitude of the possible impact of such large particles on the R_g values determined via the Guinier fits of the SAXS data, we simulated the structure of a hypothetical protein aggregate consistent with the ~ 80 nm size extracted from DLS measurements (Figure S9d). Close packing of the members of the ensemble determined via the SAXS/FRET fit of the R17d data in 1 M GdmCl results in aggregates containing ~ 27 000 monomeric subunits. The scattering profiles predicted for such particles fall off by ~ 4 orders of magnitude from the zero scattering angle to $q = 0.005 \text{ \AA}^{-1}$ and lead to changes in the fitted R_g not exceeding 0.02–0.03 nm, well below our experimental uncertainties.

In summary, all four experimental techniques we employed expose a clear change in unfolded state expansion with increasing denaturant concentration for both proteins and both denaturants investigated (i.e., 16 different combinations). However, the relative changes in the quantities accessible from the different methods are significantly different (Table S2), raising the question whether these results can be accounted for consistently. We analyzed all experiments by using standard techniques with the simplest possible models. However, each experiment carries its own uncertainties due to the way the data are interpreted. For example, FRET experiments must employ a specific model to obtain the distribution of donor–acceptor distances $P(r)$ over which the transfer efficiency is averaged. With SAXS, the extraction of the radius of gyration from raw data is relatively model free. In practice, however, it is complicated by the narrow range of the Guinier region for a heterogeneous ensemble, the large experimental noise at the low protein concentrations necessary to ensure the absence of interparticle repulsion or protein association effects, as well as at higher denaturant concentrations due to poorer protein/solvent contrast. Ideally, one would use all of the available scattering data to estimate the molecular size. However, model-free analysis of the wider angle data is more challenging: The distance distribution function, $P(r)$, and the associated R_g are commonly calculated via a regularized Fourier transform, which creates a regularizer bias toward distributions characteristic of globular folded particles and may thus be ill suited for the analysis of structurally diverse IDPs. Accurate extraction of R_g via $P(r)$ methods is further complicated by the inevitable underestimation of the maximum dimensions for an unfolded protein, motivating the development of ensemble refinement methods.⁷⁶ Alternatively, wide-angle data can be fitted to the Debye analytical expression for a Gaussian chain,⁷⁷ but our scaling exponent data suggest deviations from Θ conditions in most cases, and the Debye model is known to fit poorly for chains with excluded volume at larger q .⁷⁸ Lastly, we would ideally like to compare the results for R , R_g , and R_h more directly, and there is no generally applicable analytical relation between them. Is there a way to obtain all of the desired parameters by employing the different experimental data at our disposal and concomitantly to overcome the inherent uncertainties and limitations of each individual technique?

Bayesian Reweighting of Structure Ensembles. One way to achieve all of these goals is to use an explicit molecular model that accounts for the expected conformational heterogeneity of unfolded proteins. Such approaches using ensembles of structures have previously been successful in interpreting combinations of many types of data, including those from SAXS, NMR, EPR, and FRET experiments.^{79–84} Here, we approach this task by first generating a trial initial ensemble via simulations with the ABSINTH implicit solvent model.⁸⁵ The SAXS intensity for each structure in the initial ensemble is then calculated with CRY SOL,⁸⁶ in which the default background electron density and hydration shell are used. A comparison between the SAXS calculation using continuum or atomistic representations of solvent can be found in a related work,⁷² showing that the continuum model reproduces excellently the Guinier region of SAXS intensity ($q < 0.04 \text{ \AA}^{-1}$) and the corresponding R_g , so that any effects of solvent structure must have little impact on R_g . FRET efficiencies are calculated for each structure using the Förster relation.⁵⁷ We then apply a reweighting procedure to achieve agreement with the experimental data using the EROS

method.^{62,81} A key feature of the analysis is a regularization procedure to prevent overfitting of the data to the very large number of structures in the initial ensemble relative to the number of experimental data^{76,81,87–90} (described in SI text and Figure S10).

To test whether we are able to recover a representative ensemble, we first applied the procedure to synthetic FRET efficiencies and SAXS intensities calculated from all-atom, explicit solvent simulations of ACTR in urea,⁷² in which case the true properties of the molecular ensemble are known. We find that the distributions of R_g , R , and R_h recovered from the reweighting of the implicit-solvent model to match the synthetic FRET and SAXS data agree very well with those estimated directly from the all-atom simulations⁷² (much better than the unweighted implicit solvent models) (Figure S11). Note that the differences between SAXS curves calculated from simulations with increasing denaturant concentrations are quite subtle, as in experiment, yet associated with a clear increase in R_g .

We thus applied the same Bayesian ensemble reweighting approach to a joint analysis of the FRET and SAXS data, whose quantitative relation to the structure ensemble is more straightforward than for hydrodynamic data. In Figure 5a, we show examples of the quality of fit and residuals for the reweighted ensembles for R17d and ACTR SAXS data in GdmCl (results for urea are given in Figure S12), and in Figure 5b the quality of the fit to the FRET data using multiple labeling positions. We find that we are able to fit both data sets very well, showing that they are mutually compatible. There is a small deviation from the experimental SAXS data for $q > 0.1 \text{ \AA}^{-1}$; however, differences are expected at larger q due to the lack of a realistic model of solvent structure: a comparison of a SAXS calculation using both protein and solvent molecules from an all-atom simulation with one using only the protein and a continuum solvent model also starts to show deviations at $q \approx 0.1 \text{ \AA}^{-1}$.⁷² Below this q , however, both calculations give very similar results, demonstrating that a detailed solvent model is not required to account for this low q range.⁷²

The distributions of r_g from the resulting ensembles reweighted using the experimental data, shown in Figure 5c, reveal a systematic expansion with increasing denaturant concentration. We note that this expansion is determined both by the SAXS and by the FRET data: separate reweighted ensembles using only SAXS or only FRET data recover a similar trend in R_g to that from the combined fit (Figure S13). The consistency with the R_g from the ensembles determined using only one type of data also shows that the ensemble using both SAXS and FRET is not simply “interpolating” between the data sets, but rather, both experiments are pointing to the same outcome. An additional independent test of the molecular ensembles is their comparison with the results from 2f-FCS and DLS. Thus, we computed hydrodynamic radii from the reweighted ensembles determined by reweighting based on FRET and SAXS data with the shell model in the program HydroPro.⁷⁴ As shown in Figure 4, these back-calculated hydrodynamic radii (and especially their changes with denaturant concentration) are in reasonable agreement with those estimated from 2f-FCS and DLS measurements, further cross-validating the simulated ensembles and indicating the consistency of all four experimental techniques used. Accompanying the increase of R_g and R_h is a modest increase in asphericity (Figure S14) with increasing denaturant concentration, consistent with theoretical expectations.^{66,91}

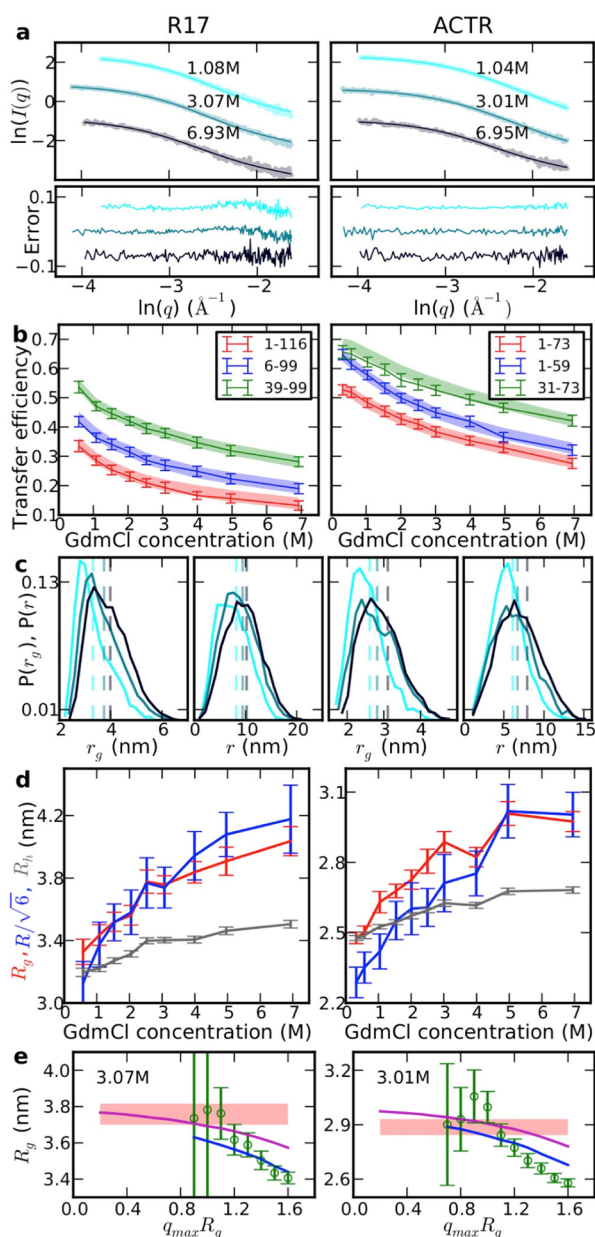


Figure 5. Results from refined ensembles using SAXS and FRET data of R17d (left) and ACTR (right) in GdmCl. (a) Examples of calculated scattering curves from the ensemble model compared to SAXS data in GdmCl and residuals (below). (b) FRET efficiencies calculated from the same models compared to experimental results for three different sets of labeling positions (see legend for label positions). Shaded bands represent experimental data (width of bands corresponding to systematic error). (c) Variation of r_g and end-to-end distance (r) distributions of ensembles for different denaturant concentrations (colors as labeled in a). The corresponding root-mean-square end-to-end distances, R , are shown as vertical dashed lines. (d) R_g , R , and R_h from the reweighted ensembles as a function of GdmCl concentration. We plot $R/\sqrt{6}$ to place R on the same scale as R_g and R_h . (e) Variation of R_g from Guinier fits as a function of $q_{\max}R_g$ for direct fits to experimental scattering curves (green symbols and error bars), the $I(q)$ calculated from the reweighted ensemble starting at $q = 0$ (purple line) and starting at the smallest q accessible experimentally (blue line), and the actual R_g computed from the ensemble coordinates (red shaded region with a width corresponding to the uncertainty based on posterior sampling of the ensemble space). Corresponding results for urea are shown in Figure S12.

We also tested whether the ensemble analysis is sensitive to the consistency of the experimental data sets with each other. To do this we combined the ACTR SAXS data from the present work with FRET data collected with some of the most hydrophobic chromophores available for FRET (as quantified by reversed-phase HPLC, Figure S15), Atto 647N and Abberior STAR 635. In the absence of denaturant, a pronounced increase in FRET efficiency was observed for ACTR labeled with these dyes, indicating further collapse relative to the commonly employed hydrophilic dyes containing charged groups (e.g., Alexa Fluor 488 and 594, Table S3). While it is possible to select a subensemble which fits both SAXS and FRET data using the hydrophobic dyes, there are two indications that the fit is poor (Table S4): First, a much stronger reweighting of the original ensemble is required, as measured by the lower fit entropy, compared to when the data based on the hydrophilic dyes are used. Second, if only the SAXS data are used to reweight the simulations, FRET for the hydrophilic chromophore pairs is in reasonable agreement with experiment, but the agreement for the hydrophobic chromophore pairs is poor. Similarly, if only the FRET data are used for reweighting, reasonable agreement with the SAXS data is obtained for the hydrophilic dye pair but not for the hydrophobic dyes. In summary, the analysis used here not only provides molecular ensembles compatible with all experimental data used but also enables inconsistent experimental results to be identified.

DISCUSSION

Overall, the results from all of the methods we employed indicate an expansion of the polypeptide chain with increasing denaturant concentration and are mutually compatible. To illustrate this consistency, we show in Figure 6 the denaturant dependencies of R and R_g from the direct analysis of the FRET and/or SAXS experiments as well as from the reweighted ensembles. In all cases, we find an expansion with increasing denaturant concentration, with the most pronounced changes occurring at the lower denaturant concentrations. The steeper increase in R_g at lower denaturant concentrations is consistent with the expectations of a binding model of denaturant interactions (where saturation must occur at some point) and with previous FRET studies on unfolded and intrinsically disordered proteins.^{6,35,58,92} Similarly, the polymer scaling exponents increase with denaturant concentration, whether estimated from FRET, SAXS fractal dimension, or the dependence of the intramolecular distances on the sequence separation in the reweighted ensembles (Figures 2 and 3; Figure S16).

While all of the experimental data indicate an expansion with increasing denaturant concentration, the ensembles resulting from our analysis illustrate a noteworthy difference in the denaturant sensitivity of the observables monitored (Figure 5d): over the experimentally accessible denaturant ranges, the increase in R is 28–43%, in R_g 20–29%, and in R_h only 9–11% (ranges denote the largest and smallest change across all protein/denaturant combinations (Table S2)). A corresponding analysis of conformational ensembles from unbiased molecular simulations of ACTR yields similar trends (Table S2). These different measures of chain size thus exhibit different relative amplitudes upon expansion or collapse. Since FRET measurements are most directly related to R , the transfer efficiency is intrinsically most responsive to chain expansion. These differences in relative amplitudes are expected from

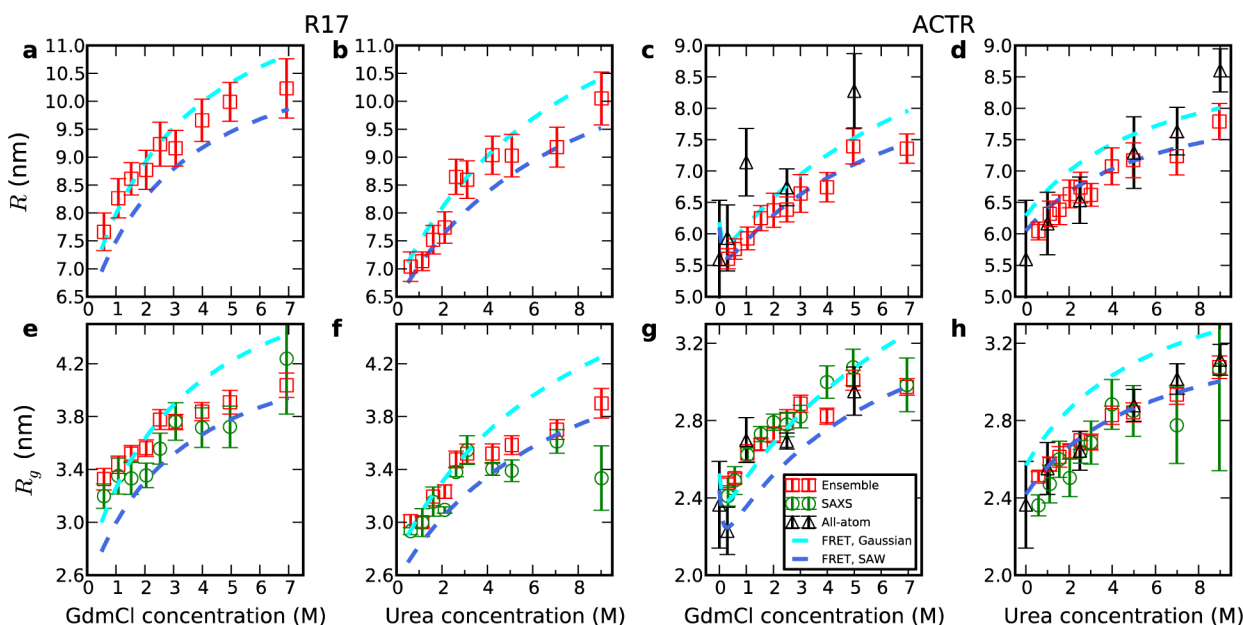


Figure 6. Denaturant-induced expansion of R17d and ACTR as seen from multiple methods. (a–d) Average end-to-end distances R in GdmCl and urea for R17d and ACTR. (e–h) Corresponding radii of gyration. Data are from a Guinier analysis of SAXS data with $q_{\max}R_g \leq 1.11$ (green), from the analysis of FRET data with the Gaussian chain model as an upper bound (cyan) and a self-avoiding walk (SAW) as a lower bound (blue), from the ensemble refinement (red), and from all-atom molecular dynamics simulations of ACTR (black).⁷²

polymer theory, simulations, and previous experiments. Specifically, an increase in the ratio R/R_g is predicted upon expansion of polymers from Θ to good-solvent conditions by renormalization group theory⁶⁸ and from simulations of homopolymers⁹³ and unfolded proteins,⁶⁵ as the effective attraction between monomers is reduced. R_g is also expected to exhibit a larger change upon expansion than R_h from theory,^{68,94} simulations,⁹⁵ and experiments on homopolymers.⁷³ The sensitivity of FRET is further amplified by the highly nonlinear distance dependence of the transfer efficiency E , such that E changes are larger than 50% from the lowest to the highest denaturant concentration in all cases. The combination of these effects helps to explain why unfolded state expansion has invariably been detected in single-molecule FRET experiments. However, why do we observe an increase in R_g using SAXS while such an expansion was not resolved in some earlier studies?

As our data illustrate, detecting changes of R_g from SAXS data is challenging due to the subtle variations in the shape of $I(q)$ with denaturant concentration and the large associated errors for each data set (Figure S5), as previously suggested.⁴² The trend becomes clear only with repeated independent data collections for each combination of protein and denaturant concentration, sampling a sufficiently large number of denaturant concentrations, and careful control of the effects of interparticle interference and protein self-association. The latter necessitates the use of low protein concentrations, requiring high flux of the incident beam. Even with the undulator beamline and third-generation synchrotron source at the Argonne National Laboratory, the dependence of R_g on denaturant concentration is noisy, particularly at the higher denaturant concentrations, where the decreased protein/buffer contrast and higher X-ray absorption increase the uncertainty of the experimental data. Both a reduction of the applicable range of the Guinier approximation with the expansion of the protein at higher denaturant concentration and the lack of reliable

lowest q data reduce the apparent fitted R_g progressively as the denaturant concentration increases. A systematic analysis of the validity of the Guinier fit to the primary SAXS data is challenging because of the experimental noise, but we can use the smooth $I(q)$ calculated from the structure ensembles to illustrate this point: in Figure 5e we show the dependence of the Guinier-fitted R_g on $q_{\max}R_g$. If the fit is started from $q = 0$ then the systematic error of the fit reaches ~ 0.1 nm for $q_{\max}R_g \approx 0.9$. However, if the fit is started at the q corresponding to the first experimental data point (always $q > 0$), the underestimation of R_g is even greater (blue curve in Figure 5e). Finally, for equilibrium SAXS measurements, reliable radii of gyration can only be extracted well above the denaturation midpoint, due to the difficulty of accounting for native state scattering at lower denaturant concentration.^{18–20} Our results are in fact consistent with the earlier findings of little variation in R_g above typical midpoint denaturant concentrations.²³

To illustrate the difficulty of observing an R_g change at high denaturant concentration, we fit the dependence of R_g from the SAXS Guinier region on denaturant concentration (Figure 6) with two linear models: one with both slope and intercept as free parameters, and the other with only the intercept as a free parameter and the slope fixed to zero. Since the model with two parameters always fits better, we introduce the Bayesian information criterion (BIC)⁹⁶ to evaluate whether the fit is significantly better if the slope is not fixed to zero. In Table S5, we show that if we fit R_g over all denaturant concentrations, the BIC score indicates with high significance that the two-parameter model with nonzero denaturant dependence is better. However, when restricting the fit to data from denaturant concentrations above 3 M (urea or GdmCl), in three of the four cases the SAXS data fail to indicate a statistically meaningful change of R_g with denaturant concentration, and in the fourth (ACTR in GdmCl), the improvement when including denaturant dependence of R_g is of marginal significance. These results stress the importance of

making as many measurements of R_g over as wide a range of denaturant conditions as possible in order to have the best chance of resolving any variation. In principle, for stably folded proteins, time-resolved SAXS measurements could provide access to the low-denaturant region, where we find R_g expansion to be most prominent. However, in most cases time-resolved SAXS measurements also suggest no collapse after denaturant dilution, even when the final denaturant concentration is very low.^{21–24} We cannot comment directly on these results except to note that these measurements, performed with very short exposures, would have even larger errors than static scattering data.

The potential presence of small amounts of aggregates or other larger particles in the sample may distort the R_g extracted from the SAXS measurements. To mitigate this problem, we first selected highly soluble proteins, and second used sample aliquots coming from the exact same batch (i.e., identical samples) for SAXS and DLS experiments, following the same handling protocols for both techniques, as described in the [Supporting Information](#). In this way, we were able to use the exquisite sensitivity of DLS to aggregation to determine that we always had $\leq 1\%$ of slow-diffusing particles in our samples at every denaturant concentration. Simulations of the effect of hypothetical protein aggregates consistent with the ~ 80 nm size extracted from DLS measurements show the effect on SAXS data to be negligible in that range. We note, however, that higher concentrations of aggregates could lead to an overestimation of R_g , especially at the lowest denaturant concentrations, where aggregation is most likely to occur.

A potential complication in FRET experiments is whether the extrinsic fluorophores themselves influence the results, perhaps inducing collapse, although molecular simulations suggest this to be a small effect.^{72,97} To probe for this contribution, we tested some of the most hydrophobic chromophores currently available, which lead to a pronounced additional collapse of ACTR in the absence of denaturant. However, the resulting transfer efficiencies are incompatible with our SAXS data in the sense that the structural ensembles produced using both the SAXS data and the hydrophobic dyes require rather extreme reweighting, and ensembles produced with SAXS or FRET alone do not reproduce the respective other data set ([Table S4](#)). In contrast, the SAXS data are consistent with the FRET data collected from the protein labeled with the hydrophilic dyes used here and in many other experiments. Further direct evidence for the absence of an effect from the labels comes from the agreement of the 2f-FCS results on labeled protein with the DLS measurements on unlabeled protein, indicating at most a modest R_h increase, possibly due to the contribution of the fluorophores to the protein mass (+6% or +10% for R17d or ACTR, respectively). Lastly, in many experiments using identical dye pairs, large differences in FRET-based intramolecular distances have been observed for different polypeptide sequences, demonstrating that changes in the charge composition and hydrophobicity of the polypeptide chain itself are dominant over any effects from the fluorophores.^{40,63,98}

For a quantitative determination of average distance, R , and radius of gyration, R_g , from single-molecule FRET and comparison with SAXS without using ensemble refinement, important considerations are the uncertainty in the transfer efficiency and the need to assume a specific polymer model. From more than a decade of measurements in our laboratory, using different instruments and dye pairs, we estimate an

accuracy in the transfer efficiency, ΔE , of ~ 0.02 , mainly arising from instrument calibration and other corrections; the precision of transfer efficiency measurements performed on a single instrument on the same day is < 0.005 . Therefore, the greater challenge for the quantitative interpretation of single-molecule FRET experiments on unfolded proteins is the model dependence of the conversion of E to R and R_g . Our results indicate that using the $P(r)$ of simple polymer models may overestimate the degree of expansion. As pointed out previously, using $P(r)$ of a Gaussian chain leads to an overestimation of chain dimensions by $\sim 10\%$ at the highest denaturant concentrations⁶⁵ but often provides a better approximation at low denaturant ([Figure 6](#)). On the other hand, $P(r)$ of a SAW tends to underestimate chain dimensions at low denaturant concentrations but provides a better approximation at high denaturant concentrations ([Figure 6](#)). Given the crossover⁹⁹ from Θ to good solvent conditions during denaturant-induced chain expansion,⁴⁰ this observation is not entirely surprising and can contribute to the apparent discrepancy with SAXS results. Using the distance distribution of a SAW, we find that we are able to more accurately recover the distance R and radius of gyration R_g from the transfer efficiency when applied to synthetic data from simulations ([Figure S4](#)). In the absence of molecular simulations for ensemble refinement, polymer models thus provide useful estimates of intramolecular distance distributions, but the choice of the model leads to a variability of $\sim 10\%$ in chain dimensions ([Figure 6](#)). The conversion of R to R_g involves additional assumptions regarding the ratio of the two quantities, which depends on solvent quality,^{68,99} and thus introduces additional uncertainty.

Because of the controversy we aim to address, our analysis has been focused mainly on the radius of gyration and related quantities that probe large-scale features and overall dimensions of the sampled molecular conformations. Obtaining a consistent value of this most basic property of an unfolded or disordered protein states, when measured by different techniques, is clearly a prerequisite for developing structural models for these states. Nonetheless, the ensemble of states populated by an IDP or unfolded protein cannot always be reduced to a description in terms of simple polymer theories, and specific local interactions and structure may be important in many cases.^{100,101} Resolving the apparent disagreement between SAXS and FRET experiments opens the way to the integration of both types of data in detailed structural models of disordered proteins.

CONCLUSIONS

Previously, qualitative discrepancies regarding the effect of chemical denaturants on the dimensions of unfolded and disordered proteins have been reported when comparing the results from SAXS and other experimental methods, especially FRET. However, the two methods had previously only been applied to one protein in common, protein L. In the present work, by comparing two different proteins in two different denaturants and using four different experimental methods, we find that all results are self-consistent and show an increase of the average distance between FRET labels, radius of gyration, polymer scaling exponent, and hydrodynamic radius of the chains with increasing denaturant concentration. These findings are consistent with expectations based on the improved solvent quality in concentrated denaturant solutions.^{33,42,43,49,50,102,103}

We stress that while the proteins considered here do collapse as the denaturant concentration is reduced, they do not form a fully collapsed globule in water.^{6,35,58,92} Instead, they populate a partially compacted ensemble close to the Θ state, in which protein and solvent interactions are balanced, a situation also obtained for other proteins.^{40,44} A careful analysis of our results helps to explain the apparent discrepancies in earlier work. First, the FRET efficiency is inherently more sensitive to changes in protein expansion, due to the greater relative change of R with denaturant than R_g or R_h and due to the nonlinear distance dependence of FRET. In addition, the use of polymer-based distance distributions for obtaining average distance and radius of gyration from FRET can lead to an overestimation of the degree of chain expansion with denaturant. On the other hand, probing expansion by SAXS is complicated by several factors, which may lead to an underestimation, including most prominently (i) the sensitivity of R_g to the fitting range used in the Guinier analysis and (ii) the difficulty of determining R_g at the lowest denaturant concentrations, where the largest changes in protein dimensions occur, in equilibrium ensemble-averaged techniques such as SAXS that are restricted to measurements sufficiently far above the unfolding midpoint. The integrated experimental approach presented here, combined with Bayesian ensemble refinement, suggests a plausible resolution to a long-standing controversy.

■ ASSOCIATED CONTENT

Supporting Information

The Supporting Information is available free of charge on the ACS Publications website at DOI: 10.1021/jacs.6b05917.

Description of experiment and simulation methods, data analysis, and additional figures (PDF)

■ AUTHOR INFORMATION

Corresponding Authors

*schuler@bioc.uzh.ch
*a.borgia@bioc.uzh.ch
*khpghost@uni-potsdam.de
*alexander.grishaev@nist.gov
*robertbe@helix.nih.gov

Present Address

◇Department of Structural Biology, Weizmann Institute of Science, Rehovot, Israel.

Author Contributions

§These authors contributed equally to this work.

Notes

The authors declare no competing financial interest.

■ ACKNOWLEDGMENTS

We thank Ad Bax, William Eaton, Gilad Haran, and Dave Thirumalai for helpful comments and suggestions, Jane Clarke for an expression plasmid for R17, Franziska Zosel for a high-yield expression plasmid for ACTR, and Andrea Holla for help in identifying suitable alternative FRET pairs. R.B. and W.Z. were supported by the intramural research program of the National Institute of Diabetes and Digestive and Kidney Diseases of the National Institutes of Health. This work utilized the computational resources of the NIH HPC Biowulf cluster (<http://hpc.nih.gov>). Work at the University of Zurich was supported by funding from the Swiss National Science foundation and the European Research Council. For the

SAXS experiments, we gratefully acknowledge use of the SAXS Core Facility of Center for Cancer Research, National Cancer Institute (NCI). Scattering data were acquired using the shared scattering beamline 12-ID-B resource allocated under the PUP-24152 agreement between the National Cancer Institute and Argonne National Laboratory (ANL). We thank Dr. Lixin Fan (NCI) and Dr. Xiaobing Zuo (ANL) for their expert support. The Advanced Photon Source, a U.S. Department of Energy (DOE) Office of Science User Facility, is operated for the DOE Office of Science by Argonne National Laboratory under Contract No. DE-AC02-06CH11357.

■ REFERENCES

- (1) Wolynes, P. G.; Onuchic, J. N.; Thirumalai, D. *Science* **1995**, *267*, 1619.
- (2) Bryngelson, J. D.; Wolynes, P. G. *Proc. Natl. Acad. Sci. U. S. A.* **1987**, *84*, 7524.
- (3) Leopold, P. E.; Montal, M.; Onuchic, J. N. *Proc. Natl. Acad. Sci. U. S. A.* **1992**, *89*, 8721.
- (4) Šali, A.; Shakhnovich, E. I.; Karplus, M. *Nature* **1994**, *369*, 248.
- (5) Dill, K. A.; Chan, H. S. *Nat. Struct. Biol.* **1997**, *4*, 10.
- (6) Schuler, B.; Eaton, W. A. *Curr. Opin. Struct. Biol.* **2008**, *18*, 16.
- (7) Theillet, F.-X.; Binolfi, A.; Frembgen-Kesner, T.; Hingorani, K.; Sarkar, M.; Kyne, C.; Li, C.; Crowley, P. B.; Gierasch, L.; Pielak, G. J.; Elcock, A. H.; Gershenson, A.; Selenko, P. *Chem. Rev.* **2014**, *114*, 6661.
- (8) Van der Lee, R.; Buljan, M.; Lang, B.; Weatheritt, R. J.; Daughdrill, G. W.; Dunker, A. K.; Fuxreiter, M.; Gough, J.; Gsponer, J.; Jones, D. T.; Kim, P. M.; Kriwacki, R. W.; Oldfield, C. J.; Pappu, R. V.; Tompa, P.; Uversky, V. N.; Wright, P. E.; Babu, M. M. *Chem. Rev.* **2014**, *114*, 6589.
- (9) Mittag, T.; Orlicky, S.; Choy, W.-Y.; Tang, X.; Lin, H.; Sicheri, F.; Kay, L. E.; Tyers, M.; Forman-Kay, J. *Proc. Natl. Acad. Sci. U. S. A.* **2008**, *105*, 17772.
- (10) Marsh, J. A.; Dancheck, B.; Ragusa, M. J.; Allaire, M.; Forman-Kay, J.; Peti, W. *Structure* **2010**, *18*, 1094.
- (11) Michalek, X.; Weiss, S.; Jäger, M. *Chem. Rev.* **2006**, *106*, 1785.
- (12) Schuler, B.; Hofmann, H. *Curr. Opin. Struct. Biol.* **2013**, *23*, 36.
- (13) Meier, S.; Blackledge, M.; Grzesiek, S. *J. Chem. Phys.* **2008**, *128*, 052204.
- (14) Graewert, M. A.; Svergun, D. I. *Curr. Opin. Struct. Biol.* **2013**, *23*, 748.
- (15) Nöppert, A.; Gast, K.; Müller-Frohne, M.; Zirwer, D.; Damaschun, G. *FEBS Lett.* **1996**, *380*, 179.
- (16) Dertinger, T.; Pacheco, V.; Von der Hocht, I.; Hartmann, R.; Gregor, I.; Enderlein, J. *ChemPhysChem* **2007**, *8*, 433.
- (17) Doose, S.; Neuweiler, H.; Sauer, M. *ChemPhysChem* **2009**, *10*, 1389.
- (18) Smith, C. K.; Bu, Z.; Anderson, K. S.; Sturtevant, J. M.; Engelman, D. M.; Regan, L. *Protein Sci.* **1996**, *5*, 2009.
- (19) Flanagan, J. M.; Kataoka, M.; Fujisawa, T.; Engelman, D. M. *Biochemistry* **1993**, *32*, 10359.
- (20) Choy, W.-Y.; Mulder, F. A. A.; Crowhurst, K. A.; Muhandiram, D. R.; Millett, I. S.; Doniach, S.; Forman-Kay, J. D.; Kay, L. E. *J. Mol. Biol.* **2002**, *316*, 101.
- (21) Plaxco, K. W.; Millett, I. S.; Segel, D. J.; Doniach, S.; Baker, D. *Nat. Struct. Biol.* **1999**, *6*, 554.
- (22) Watkins, H. M.; Simon, A. J.; Sosnick, T. R.; Lipman, E. A.; Hjelm, R. P.; Plaxco, K. W. *Proc. Natl. Acad. Sci. U. S. A.* **2015**, *112*, 6631.
- (23) Yoo, T. Y.; Meisburger, S. P.; Hinshaw, J.; Pollack, L.; Haran, G.; Sosnick, T. R.; Plaxco, K. *J. Mol. Biol.* **2012**, *418*, 226.
- (24) Jacob, J.; Krantz, B.; Dothager, R. S.; Thiagarajan, P.; Sosnick, T. R. *J. Mol. Biol.* **2004**, *338*, 369.
- (25) Johansen, D.; Trewthella, J.; Goldenberg, D. P. *Protein Sci.* **2011**, *20*, 1955.10.1002/pro.739
- (26) Kimura, T.; Akiyama, S.; Uzawa, T.; Ishimori, K.; Morishima, I.; Fujisawa, T.; Takahashi, S. *J. Mol. Biol.* **2005**, *350*, 349.

- (27) Uzawa, T.; Kimura, T.; Ishimori, K.; Morishima, I.; Matsui, T.; Ikeda-Saito, M.; Takahashi, S.; Akiyama, S.; Fujisawa, T. *J. Mol. Biol.* **2006**, *357*, 997.
- (28) Konuma, T.; Kimura, T.; Matsumoto, S.; Goto, Y.; Fujisawa, T.; Fersht, A. R.; Takahashi, S. *J. Mol. Biol.* **2011**, *405*, 1284.
- (29) Deniz, A. A.; Laurence, T. A.; Beligere, G. S.; Dahan, M.; Martin, A. B.; Chemla, D. S.; Dawson, P. E.; Schultz, P. G.; Weiss, S. *Proc. Natl. Acad. Sci. U. S. A.* **2000**, *97*, 5179.
- (30) Schuler, B.; Lipman, E. A.; Eaton, W. A. *Nature* **2002**, *419*, 743.
- (31) Sherman, E.; Haran, G. *Proc. Natl. Acad. Sci. U. S. A.* **2006**, *103*, 11539.
- (32) Möglich, A.; Joder, K.; Kiefhaber, T. *Proc. Natl. Acad. Sci. U. S. A.* **2006**, *103*, 12394.
- (33) Ziv, G.; Haran, G. *J. Am. Chem. Soc.* **2009**, *131*, 2942.
- (34) Soranno, A.; Longhi, R.; Bellini, T.; Buscaglia, M. *Biophys. J.* **2009**, *96*, 1515.
- (35) Haran, G. *Curr. Opin. Struct. Biol.* **2012**, *22*, 14.
- (36) Buscaglia, M.; Lapidus, L. J.; Eaton, W. A.; Hofrichter, J. *Biophys. J.* **2006**, *91*, 276.
- (37) Holthauzen, L. M. F.; Rösger, J.; Bolen, D. W. *Biochemistry* **2010**, *49*, 1310.
- (38) Guo, L.; Chowdhury, P.; Glasscock, J. M.; Gai, F. *J. Mol. Biol.* **2008**, *384*, 1029.
- (39) Sherman, E.; Itkin, A.; Kuttner, Y. Y.; Rhoades, E.; Amir, D.; Haas, E.; Haran, G. *Biophys. J.* **2008**, *94*, 4819.
- (40) Hofmann, H.; Soranno, A.; Borgia, A.; Gast, K.; Nettels, D.; Schuler, B. *Proc. Natl. Acad. Sci. U. S. A.* **2012**, *109*, 16155.
- (41) Kaplon, T. M.; Michnik, A.; Drzazga, Z.; Richter, K.; Kochman, M.; Ozyhar, A. *Biochim. Biophys. Acta, Proteins Proteomics* **2009**, *1794*, 1616.
- (42) Liu, Z.; Reddy, G.; Thirumalai, D. *J. Phys. Chem. B* **2016**, in press.10.1021/acs.jpcc.6b00327
- (43) O'Brien, E.; Ziv, G.; Brooks, B. R.; Thirumalai, D. *Proc. Natl. Acad. Sci. U. S. A.* **2008**, *105*, 13403.
- (44) Wang, Y.; Trehwella, J.; Goldenberg, D. P. *J. Mol. Biol.* **2008**, *377*, 1576.
- (45) Merchant, K. A.; Best, R. B.; Louis, J. M.; Gopich, I. V.; Eaton, W. A. *Proc. Natl. Acad. Sci. U. S. A.* **2007**, *104*, 1528.
- (46) Knowles, D. B.; Shkel, I.; Phan, N. M.; Sternke, M.; Lingeman, E.; Cheng, X.; Cheng, L.; O'Connor, K.; Record, M. T. *Biochemistry* **2015**, *54*, 3528.
- (47) Uversky, V. N.; Gillespie, J. R.; Millett, I. S.; Khodyakova, A. V.; Vasiliev, A. M.; Chernovskaya, T. V.; Vasilenko, R. N.; Kozlovskaya, G. D.; Dolgikh, D. A.; Fink, A. L.; Doniach, S.; Abramov, V. M. *Biochemistry* **1999**, *38*, 15009.
- (48) Sosnick, T. R.; Trehwella, J. *Biochemistry* **1992**, *31*, 8329.
- (49) Frank, H. S.; Franks, F. *J. Chem. Phys.* **1968**, *48*, 4746.
- (50) Nozaki, Y.; Tanford, C. *J. Biol. Chem.* **1963**, *238*, 4074.
- (51) Demarest, S. J.; Martinez-Yamout, M.; Chung, J.; Chen, H.; Xu, W.; Dyson, H. J.; Evans, R. M.; Wright, P. E. *Nature* **2002**, *415*, 549.
- (52) Soranno, A.; Koenig, I.; Borgia, M. B.; Hofmann, H.; Zosel, F.; Nettels, D.; Schuler, B. *Proc. Natl. Acad. Sci. U. S. A.* **2014**, *111*, 4874.
- (53) Kjaergaard, M.; Teilum, K.; Poulsen, F. M. *Proc. Natl. Acad. Sci. U. S. A.* **2010**, *107*, 12535.
- (54) Borgia, A.; Wensley, B. G.; Soranno, A.; Nettels, D.; Borgia, M. B.; Hoffmann, A.; Pfeil, S. H.; Lipman, E. A.; Clarke, J.; Schuler, B. *Nat. Commun.* **2012**, *3*, 1195.
- (55) Kjaergaard, M.; Norholm, A.-B.; Hendus-Altenburger, R.; Pedersen, S. F.; Poulsen, F. M.; Kragelund, B. B. *Protein Sci.* **2010**, *19*, 1555.
- (56) Scott, K. A.; Batey, S.; Hooton, K. A.; Clarke, J. *J. Mol. Biol.* **2004**, *344*, 195.
- (57) Förster, T. *Ann. Phys.* **1948**, *437*, 55.
- (58) Schuler, B.; Hofmann, H.; Nettels, D.; Soranno, A. *Annu. Rev. Biophys.* **2016**, *45*, 207.
- (59) Lipfert, J.; Doniach, S. *Annu. Rev. Biophys. Biomol. Struct.* **2007**, *36*, 307.
- (60) Putnam, C. D.; Hammel, M.; Hura, G. L.; Tainer, J. A. *Q. Rev. Biophys.* **2007**, *40*, 191.
- (61) Gast, K.; Modler, A. J. In *Protein Folding Handbook*; Buchner, J., Kiefhaber, T., Eds.; Wiley-VCH: Weinheim, 2005; Vol. 2, p 673.
- (62) Köfinger, J.; Hummer, G. *J. Chem. Phys.* **2015**, *143*, 243150.
- (63) Müller-Späh, S.; Soranno, A.; Hirschfeld, V.; Hofmann, H.; Ruegger, S.; Reymond, L.; Nettels, D.; Schuler, B. *Proc. Natl. Acad. Sci. U. S. A.* **2010**, *107*, 14609.
- (64) Laurence, T. A.; Kong, X.; Jäger, M.; Weiss, S. *Proc. Natl. Acad. Sci. U. S. A.* **2005**, *102*, 17348.
- (65) O'Brien, E.; Morrison, G.; Brooks, B. R.; Thirumalai, D. *J. Chem. Phys.* **2009**, *130*, 124903.
- (66) Song, J.; Gomes, G.-N.; Gradinaru, C. C.; Chan, H.-S. *J. Phys. Chem. B* **2015**, *119*, 15191.
- (67) De Gennes, P.-G. *Scaling Concepts in Polymer Physics*; Cornell University Press: Ithaca and London, 1979.
- (68) Schäfer, L. *Excluded Volume Effects in Polymer Solutions as Explained by the Renormalization Group*; Springer: Berlin, 1999.
- (69) Kohn, J. E.; Millett, I. S.; Jacob, J.; Zagrovic, B.; Dillon, T. M.; Cingel, N.; Dothager, R. S.; Seifert, S.; Thiyagarajan, P.; Sosnick, T. R.; Hasan, M. Z.; Pande, V. S.; Ruczinski, I.; Doniach, S.; Plaxco, a. K. W. *Proc. Natl. Acad. Sci. U. S. A.* **2004**, *101*, 12491.
- (70) Calmettes, P.; Durand, D.; Desmadril, M.; Minard, P.; Receveur, V.; Smith, J. C. *Biophys. Chem.* **1994**, *53*, 105.
- (71) Calmettes, P.; Durand, D.; Smith, J. C.; Desmadril, M.; Minard, P.; Douillard, R. *J. Phys. IV* **1993**, *3* (C8), C8.
- (72) Zheng, W.; Borgia, A.; Buholzer, K.; Grishaev, A.; Schuler, B.; Best, R. B. *J. Am. Chem. Soc.* **2016**, in press.
- (73) Sun, S. T.; Nishio, I.; Swislow, G.; Tanaka, T. *J. Chem. Phys.* **1980**, *73*, 5971.
- (74) Ortega, A.; Amorós, D.; García de la Torre, J. *Biophys. J.* **2011**, *101*, 892.
- (75) Perez, R. B.; Tischer, A.; Auton, M.; Whitten, S. T. *Proteins: Struct., Funct., Genet.* **2014**, *82*, 3373.
- (76) Bernado, P.; Mylonas, E.; Petoukhov, M. V.; Blackledge, M.; Svergun, D. I. *J. Am. Chem. Soc.* **2007**, *129*, 5656.
- (77) Debye, P. *J. Phys. Colloid Chem.* **1947**, *51*, 18.
- (78) Peterscu, A.-J.; Receveur, V.; Calmettes, P.; Durand, D.; Smith, J. C. *Protein Sci.* **1998**, *7*, 1396.
- (79) Lange, O. F.; Lakomek, N.-A.; Fares, C.; Schröder, G. F.; Walter, K. F. A.; Becker, S.; Meiler, J.; Grubmüller, H.; Griesinger, C.; De Groot, B. L. *Science* **2008**, *320*, 1471.
- (80) Lindorff-Larsen, K.; Best, R. B.; Depristo, M. A.; Dobson, C. M.; Vendruscolo, M. *Nature* **2005**, *433*, 128.
- (81) Boura, E.; Rózycki, B.; Herrick, D. Z.; Chung, H. S.; Vecer, J.; Eaton, W. A.; Cafiso, D. S.; Hummer, G.; Hurley, J. H. *Proc. Natl. Acad. Sci. U. S. A.* **2011**, *108*, 9437.
- (82) Allison, J. R.; Rivers, R. C.; Christodoulou, J. C.; Vendruscolo, M.; Dobson, C. M. *Biochemistry* **2014**, *53*, 7170.
- (83) Schwalbe, M.; Ozenne, V.; Bibow, S.; Jaremko, M.; Gajda, M.; Ringkjøbing-Jensen, M.; Biernat, J.; Becker, S.; Mandelkow, E.; Zweckstetter, M.; Blackledge, M. *Structure* **2014**, *22*, 238.
- (84) Brookes, D. H.; Head-Gordon, T. *J. Am. Chem. Soc.* **2016**, *138*, 4530.
- (85) Vitalis, A.; Pappu, R. V. *J. Comput. Chem.* **2009**, *30*, 673.
- (86) Svergun, D.; Barberato, C.; Koch, M. H. J. *J. Appl. Crystallogr.* **1995**, *28*, 768.
- (87) Beauchamp, K. A.; Pande, V. S.; Das, R. *Biophys. J.* **2014**, *106*, 1381.
- (88) Antonov, L. D.; Olsson, S.; Boomsma, W.; Hamelryck, T. *Phys. Chem. Chem. Phys.* **2016**, *18*, 5832.
- (89) Foerster, F.; Webb, B.; Krukenberg, K. A.; Tsuruta, H.; Agard, D. A.; Sali, A. *J. Mol. Biol.* **2008**, *382*, 1089.
- (90) Yang, S.; Blachowicz, L.; Makowski, L.; Roux, B. *Proc. Natl. Acad. Sci. U. S. A.* **2010**, *107*, 15757.
- (91) Jagodzinski, O.; Eisenriegler, E.; Kremer, K. *J. Phys. I* **1992**, *2*, 2243.
- (92) Ziv, G.; Thirumalai, D.; Haran, G. *Phys. Chem. Chem. Phys.* **2009**, *11*, 83.
- (93) McCrackin, F. L.; Mazur, J.; Guttman, C. M. *Macromolecules* **1973**, *6*, 859.

- (94) Grosberg, A. Y.; Kuznetsov, D. V. *Macromolecules* **1992**, *25*, 1996.
- (95) Dunweg, B.; Reith, D.; Steinhauser, M.; Kremer, K. *J. Chem. Phys.* **2002**, *117*, 914.
- (96) Schwarz, G. *Annals of Statistics* **1978**, *6*, 461.
- (97) Zerze, G. H.; Best, R. B.; Mittal, J. *Biophys. J.* **2014**, *107*, 1654.
- (98) Wuttke, R.; Hofmann, H.; Nettels, D.; Borgia, M. B.; Mittal, J.; Best, R. B.; Schuler, B. *Proc. Natl. Acad. Sci. U. S. A.* **2014**, *111*, 5213.
- (99) Oono, Y.; Fred, K. F. *J. Phys. A: Math. Gen.* **1982**, *15*, 1931.
- (100) Francis, C. J.; Lindorff-Larsen, K.; Best, R. B.; Vendruscolo, M. *Proteins: Struct., Funct., Genet.* **2006**, *65*, 145.
- (101) Allison, J. R.; Varnai, P.; Dobson, C. M.; Vendruscolo, M. *J. Am. Chem. Soc.* **2009**, *131*, 18314.
- (102) Holehouse, A. S.; Garai, K.; Lyle, N.; Vitalis, A.; Pappu, R. V. *J. Am. Chem. Soc.* **2015**, *137*, 2984.
- (103) Zheng, W.; Borgia, A.; Borgia, M. B.; Schuler, B.; Best, R. B. *J. Chem. Theory Comput.* **2015**, *11*, 5543.

Supporting Information

Consistent View of Polypeptide Chain Expansion in Chemical Denaturants from Multiple Experimental Methods

Alessandro Borgia, Wenwei Zheng, Karin Buholzer, Madeleine B. Borgia, Anja Schöler, Hagen Hofmann, Andrea Soranno, Daniel Nettels¹, Klaus Gast, Alexander Grishaev, Robert B. Best, Benjamin Schuler

SI Text

Choice of protein variants.

Amino acid exchanges in R17 were chosen to attain the strongest destabilization with the minimal changes to the protein's sequence properties, thereby maintaining wt solubility, isoelectric point, net charge and overall hydrophobicity, as much as possible. According to these criteria, and based on results in¹, we selected the substitution L90→A, which alone causes a ~70% destabilization of the native state. In our construct, we also removed Cys 66 (R17 C66A/L90A) to avoid risks of oligomerization by disulfide bridging; this mutation causes further destabilization, as observed in ref. 2. For ACTR, only Cys residues for labeling were introduced. All protein sequences are shown in Table S1.

Mutagenesis, expression and purification of R17 and ACTR

Mutations in the R17 and ACTR genes were introduced by site-directed mutagenesis.

In the construct for FRET labeling of R17, in addition to C66A/L90A ("R17d"), cysteine residues were introduced at the N and C terminus of the R17 protein sequence: R1C and Q116C ("R17d 1-116"). A construct with C66A/L90A and Q116C was produced for singly labeled samples ("R17d 116"). DNA sequencing confirmed all mutations. All DNA constructs were in pRSET plasmids with a thrombin-cleavable N-terminal HisTag described previously³. All R17 variants (collectively called "R17" in this paragraph) were expressed in *E.coli* C41 cells and 2xYT media at 37°C, induced with 1 mM IPTG at an OD₆₀₀ of ~0.6, and grown for a further 2.5 hours. Cell pellets were harvested and resuspended in denaturing buffer: 6 M GdmCl in PBS buffer (10 mM sodium phosphate pH 7.4, 137mM NaCl, 2.7mM KCl); the soluble fraction was collected and applied to Ni-IDA resin (ABT Beads, Spain) in batch. The resin was washed twice with denaturing buffer +25 mM imidazole, and the protein was eluted from the resin with denaturing buffer +500 mM imidazole. The protein was then refolded by gradient buffer exchange on a HiLoad Superdex G75 PG (GE Healthcare) in PBS, and subsequently concentrated, filtered and its HisTag cleaved with 5 U of Thrombin (Serva) per mg of R17, for 1-2 hours at room temperature. The digested mixture was then run through a HisTrap HP 5 ml column (GE Healthcare) in denaturing buffer +25 mM imidazole to remove uncleaved protein. The digested protein was then refolded by passage over a Superdex G75 PG column in 50 mM Phosphate buffer (pH 7.0) as described above, before being purified further by loading it onto a MonoQ 5/50 GL column (GE Healthcare) and

eluting it with a gradient between 50 mM Phosphate and 50 mM Phosphate +1 M NaCl. The fractions containing exclusively R17 were selected using SDS PAGE, concentrated in a Vivaspin 6 ml ultrafiltration device with 3 kDa MWCO (GE Healthcare) and the protein mass and purity confirmed by mass spectrometry. The two additional variants R17 C66A–L6C/K99C and C66A–A39C/K99C were expressed and purified as described in reference (2).

For single-molecule FRET experiments, ACTR with an N-terminal His-tag and an HRV 3C cleavage site, was co-expressed with its natural binding partner NCBD to minimize degradation⁴; two cysteines were introduced at positions 1 and 73 (S1C/S73C), or 31 and 73 (A31C/S73C) and 1 and 59 (S1C/E59C) for the other variants, by site-directed mutagenesis (Table S1), for labeling via maleimide chemistry. BL21 *E.coli* cells were grown in LB medium (Roth) and induced with IPTG. After harvesting, the cells were resuspended in 100 mM Tris pH 8.0, supplemented with benzonase (Sigma) and protease inhibitor cocktail (cOmplete Mini, Roche) and lysed by a constant cell disrupter system. Insoluble proteins and debris were pelleted and the solution loaded onto an immobilized metal affinity chromatography column (HiTrap, GE Healthcare) at 4 °C. After washing with 50 mM Tris, pH 8.0 and 10 mM imidazole, the protein complex was eluted with a gradient from 10 mM to 500 mM imidazole. 1 μM HRV 3C protease was used to cleave the N-terminal His-tag, with concomitant dialysis against 50 mM sodium phosphate, pH 7 in a 3.5 kDa cutoff membrane (Spectrum Laboratories) overnight at 4°C. To avoid any risk of aggregation after concentrating with a spin column concentrator (Vivaspin 3kDa MWCO, GE Healthcare), the cleaved protein was supplemented with 1.5 M GdmCl and reapplied onto the HiTrap column to remove the His-tag as well as the HRV 3C protease. Fractions containing the proteins were injected into a RP-HPLC Reprosil Gold 200 C18 Column (Dr. Maisch, Germany) to remove remaining contaminants and separate ACTR and NCBD. The proteins were eluted with a gradient from an aqueous solution containing 5% acetonitrile, 0.1% trifluoroacetic acid (TFA) to 100% acetonitrile and subsequently lyophilized.

ACTR does not contain any aromatic residues, preventing accurate concentration determination by Trp or Tyr absorbance (an issue we later addressed, as explained below), thus at this stage concentration determination of the protein prior to labelling was performed with a colorimetric assay (Pierce BCA Protein Assay Kit, Thermo Scientific).

For ACTR expressed for SAXS and DLS experiments, larger protein amount were needed, therefore we applied a slightly different protocol. An avi-tag with an HRV-3C cleavage site was added to the N-terminus of the protein (without Cys mutations) to boost expression, and the His-tag with a thrombin cleavage site was placed at the C-terminus. BL21 *E.coli* cells were grown in 20g/l tryptone (BD), 10g/l yeast extract (BD), 46 mM HEPES, 86 mM NaCl, 4 mM MgSO₄, supplemented with 0.4% glucose and were induced with IPTG. To minimize degradation, cells were harvested after one hour of expression and lysed in the same way as described above. For affinity chromatography, self-packed Ni-IDA (ABT Beads, Spain) columns were used. The soluble protein fraction was applied to the column, washed with 10 column volumes (CV) of 50 mM Tris, pH7, 200 mM NaCl and 2 mM β-mercaptoethanol (washing buffer I), followed by 7 CV of the same buffer supplemented with 10 mM imidazole (washing buffer II). For elution, 5 CV of washing buffer supplemented with 500 mM imidazole were used (elution

buffer). For His-tag and avi-tag simultaneous cleavage, 4 U of thrombin per mg of ACTR and a 1:200 molar ratio of HRV-3C protease:ACTR were used during the dialysis of the protein against 50 mM Tris, pH 8, 200 mM NaCl, 1 mM EDTA (AppliChem) and 2 mM β -mercaptoethanol in a 3.5 kDa cutoff membrane at 4°C overnight. After addition of 2 mM MgCl₂, the cleaved protein was purified over a self-packed Ni-IDA column pre-equilibrated with washing buffer II to remove the cleaved His-tag and the HRV 3C protease. In the last step, the protein was purified with a RP-HPLC Reprosil Gold 200 C18 column and eluted with a gradient of acetonitrile as described above. The fractions containing exclusively ACTR were selected via mass spectrometry and lyophilized (see following paragraph for details of protein concentration determination).

Determination of ACTR extinction coefficient in the far UV

Half of the lyophilized amount of ACTR for SAXS and DLS experiments was resuspended in a precisely determined volume of 4M GdmCl, and the other half in 7M urea, both solutions buffered with 50 mM sodium phosphate pH 7. Multiple spectra of several dilutions of an aliquot of ACTR from each GdmCl or urea sample stocks were recorded and their absorbance values averaged. In combination with the protein mass (~50 mg x2) determined by analytical weighing after lyophilization, we calculated an average extinction coefficient of $\epsilon(\lambda_{225\text{ nm}}) = 4.22 \pm 0.15 \text{ (mg/ml)}^{-1}\text{cm}^{-1}$, which we used for the following concentration determinations of ACTR samples for DLS and SAXS.

Preparation of samples for DLS and SAXS

Samples volumes of R17d (0.5-1 ml) were dialyzed for ~24 hours at room temperature against 250 ml of each of the measurement buffers, prepared by dilution of freshly filtered and degassed stock solutions of urea and GdmCl (whose concentration was determined with an Abbe refractometer (Krüss, Germany)) in 50 mM sodium phosphate. In addition to different concentrations of denaturant and sodium phosphate, each dialysis solution contained 5 mM TCEP, required to minimize radiation damage in SAXS experiments. Resuspended ACTR in GdmCl and urea was dialyzed against the respective GdmCl and urea solutions concentrations for SAXS and DLS experiments as described above. The correct mass and purity were confirmed by mass spectrometry. Denaturant concentrations ranged between 0.2 and 6.95 M GdmCl, and between 0.58 and 9.02 M urea. After dialysis, the concentration and the refractive index of all protein samples were measured. Samples were then flash frozen in liquid nitrogen and stored at -80°C until being measured.

Labeling of samples for FRET and 2f-FCS

R17d 1-116 for FRET measurements was labeled with Alexa Fluor 488 (donor) and Alexa Fluor 594 (acceptor) maleimide (Molecular Probes, Inc.) according to the manufacturer's procedures. Labeling was performed in 6 M GdmCl, 50 mM Phosphate at pH 7.0. The donor dye was added in a 0.7:1 molar ratio and the reaction incubated at room temperature for 1h. Then the acceptor dye was added in a 2:1 molar ratio and the reaction incubated at 4 °C overnight; then the dyes were hydrolyzed by addition of 5 mM TCEP. The labeled material was purified by reversed phase chromatography on a RP-HPLC Reprosil

Gold 200 C18 Column (Dr. Maisch, Germany), eluting with a gradient from an aqueous solution containing 5% acetonitrile, 0.1% trifluoroacetic acid (TFA) to 100% acetonitrile. Labeling was confirmed by mass spectrometry and the correct fractions lyophilized and resuspended in 50 mM sodium phosphate. Singly-labeled protein was prepared analogously with only Alexa 488 and only Alexa 594. R17 C66–L6C/K99C and C66–A39C/K99C, for probing interdyer distances of 93 and 60 amino acids, respectively, were labeled as described in².

Lyophilized ACTR was dissolved in 50mM sodium phosphate; Alexa Fluor 488 maleimide (Thermo Scientific) dissolved in DMSO (Thermo Scientific) was added in a 1:1 molar ratio and the reaction incubated for 2-3h. The reaction was stopped by adding 100 mM β -mercaptoethanol (Roth), and 3M GdmCl was added to avoid any potential aggregation. After purification of the labeled product by RP-HPLC (with a gradient of acetonitrile as described above) and lyophilization, the protein was again dissolved in 50 mM sodium phosphate and incubated with a twofold molar excess of Alexa Fluor 594 maleimide (Thermo Scientific) for labeling of the second cysteine. After hydrolysis of unreacted dye, the doubly-labeled protein was purified from other products by RP-HPLC and lyophilized. Mass spectrometry (ESI-MS) confirmed correctly doubly-labeled ACTR.

Experimental SAXS data collection and processing

All experimental SAXS data were acquired using Beam Line 12-IDB, Advanced Photon Source (Argonne National Laboratory, Argonne, IL) using a Pilatus 2M detector positioned 2.0 m from the sample capillary in a highly offset geometry with 14 keV incident radiation resulting in an observable q -range of 0.01–0.92 \AA^{-1} . Sample/buffer match was monitored with wide angle scattering data between q of 0.9 \AA^{-1} and 2.2 \AA^{-1} using a dedicated Dectris Pilatus 300K detector. Scattered radiation on both detectors was recorded subject to a 13 keV low-energy cutoff. Q-axis mapping was done using a silver behenate standard sample. In order to minimize protein degradation, samples were stored at -80 °C until data collections, then thawed and centrifuged at 21000 g for 10 min prior to data recording. In accordance with the common handling protocol established for DLS and SAXS experiments, the times the samples spent in the liquid phase before X-ray exposure did not exceed 20 min. Stock sample concentrations ranged from 5.2 to 3.5 mg/mL. Totals of 30 sequential data frames with exposure times of 2.0 s were recorded for each measurement, with the samples kept at 25 °C. Scattering data for corresponding series of 2-3 successive two-fold dilutions were recorded for each sample, in addition to the data collection at the stock concentration. For each sample, 2-3 independent repeat measurements were performed to investigate data reproducibility. No noticeable sample/buffer mismatches were found. To prevent radiation damage, 100 μL volumes of samples and buffers were oscillating during data collection. Individual data frames were masked, corrected for the detector sensitivity, radially integrated, and normalized by the corresponding incident beam intensities and sample transmissions. The final 1D scattering profiles and their uncertainties were calculated as means and mean uncertainties over the 30 individual frames. The buffer data were then subtracted from the samples scaled by the concentration-based volume fractions. Multiple data collections at the same protein and denaturant concentration were superimposed for each sample, removing the lowest- q data showing discrepancies over the individual collections exceeding the data uncertainty. Protein concentration series data were

then analyzed for each sample/denaturant combination for the evidence of inter-particle correlation effects. All data were generally free from any such measurable effects at protein concentrations below ~4 mg/mL. Guinier fits were then performed to determine the radii of gyration. The maximum fitting q -ranges (q_{max}) are determined by selecting the largest q_{max} such that $q_{max}R_g$ was smaller than or equal to the set cut-off value. The SAXS R_g reported in **Figure 6** of the main text is with $q_{max}R_g \leq 1.1$, whereas R_g and q -range for all the other $q_{max}R_g$ cut-off values can be found in **Figure S6**.

Single-Molecule Fluorescence Instrumentation

Measurements were performed using either a custom-built confocal microscope or a Micro Time 200 confocal microscope equipped with a HydraHarp 400 counting module (Picoquant, Berlin, Germany) and an Olympus UplanApo 60 \times /1.20W objective. The donor dye was excited with a continuous wave diode laser at 485 nm (dual-mode pulsed and continuous unit LDH-D-C-485, PicoQuant) at an average power of 100 μ W at the sample, or with alternating excitation of the dyes, achieved using pulsed interleaved excitation⁵. The wavelength range used for acceptor excitation was selected with a z582/15 band pass filter (Chroma) from the emission of an SC-450-4 supercontinuum fiber laser (Fianium, UK) driven at 20 MHz, which triggers (interleaved) pulses from the 485 nm diode laser used for donor excitation. Emitted photons were collected by the microscope objective, focused onto a 100 μ m pinhole, and then separated into four channels with a polarizing beam splitter and two dichroic mirrors (585DCXR, Chroma). Photons were additionally filtered by bandpass filters (ET525/50M and HQ650/100, Chroma) before being focused onto one of four single photon avalanche detectors (Optoelectronics SPCM AQR-15, PerkinElmer, Wellesley, MA or τ -SPADs, PicoQuant, Germany).

Single-molecule FRET experiments

Single-molecule FRET efficiency histograms of doubly labeled R17: R17d 1-116, C66A–L6C/K99C, C66A–A39C/K99C, and ACTR: S1C–S73C, S1C–E59C, A31C–S73C, were acquired in samples with a protein concentration of ~50 to ~75 pM using both continuous and pulsed interleaved excitation with a resolution of 16 ps by the counting electronics (time resolution was thus limited to ~50 ps by the timing jitter of the detectors). All measurements were performed in 50 mM sodium phosphate buffer, pH 7.0, in the presence of 140 mM β -mercaptoethanol (Sigma) and 0.01% Tween 20 (Pierce) with varying concentrations of GdmCl (Pierce) or urea (Sigma). Tween 20 was used to prevent surface adhesion of the proteins, and the photoprotective agent β -mercaptoethanol was employed to minimize chromophore damage and enhance brightness. All samples were retained and their refractive index measured to determine actual denaturant concentrations.

Single-molecule data analysis

Transfer efficiencies are obtained from $E = n_A / (n_A + n_D)$, where n_D and n_A are the numbers of donor and acceptor photons in each burst corrected for background, channel crosstalk, acceptor direct excitation, differences in quantum yields of the dyes, and detection efficiencies⁶. Fluorescence anisotropies (determined for all denaturant concentrations based on the polarization-sensitive detection

in the single-molecule instrument) were below 0.12 for ACTR and 0.13 for R17d 1-116, indicating rapid orientational averaging of the fluorophores (i.e. $\kappa^2 \approx 2/3$), as usually observed for unfolded proteins^{7,8}. The energy transfer depends on the distance, r , between the dyes and on the Förster radius R_0 (calculated for the respective values of the refractive index of the solution⁹) according to $E(r) = 1 / (1 + r^6 / R_0^6)$. Since the typical timescale for unfolded chain relaxation is about 100 ns^{10,11}, much longer than the fluorescence lifetime (~ 1 ns) and much shorter than the average inter-photon time (~ 10 μ s), the mean transfer efficiency (**Figure 2 c-d**) represents an averaged value over the distribution of distances sampled by the protein, i.e.

$$\langle E \rangle = \int_0^{\infty} E(r)P(r)dr \quad (\text{S1})$$

In order to extract inter-dye distances, we assumed two different distributions, the one describing a Gaussian (or Random Walk) chain

$$P_{Gauss}(r) = 4\pi r^2 \left(\frac{3}{2\pi R^2} \right)^{3/2} e^{-\frac{3}{2} \left(\frac{r}{R} \right)^2}, \quad (\text{S2})$$

and one for a self-avoiding walk (SAW)¹²:

$$P_{SAW}(r) = 4\pi r^2 \frac{a_1}{R^3} \left(\frac{r}{R} \right)^{0.269} e^{-a_2 \left(\frac{r}{R} \right)^{2.427}}, \quad (\text{S3})$$

where R is the root-mean-square inter-dye distance of the segment probed, $a_1 = 0.299$, and $a_2 = 1.269$.

Comparison of transfer efficiencies with the average lifetimes of the donor provides a further diagnostic on how rapidly distances are sampled within a burst. For a single fixed inter-dye distance, r , the mean donor lifetime in the presence of acceptor is given by $\tau_{DA} = \tau_{DA}(r) = \tau_D(1 - E(r))$, where τ_D is the lifetime in the absence of acceptor. For a dynamic chain with probability density function $P(r)$ for the inter-dye distance, the average lifetime can be described as $\tau_{DA} = \int_0^{\infty} t I(t) dt / \int_0^{\infty} I(t) dt$ with $I(t) = I_0 \int_0^{\infty} P(r) e^{-t/\tau_D(r)} dr$, where I is the time-dependent fluorescence emission intensity. Average lifetimes are estimated by using the mean arrival time of the photons in a burst relative to the exciting laser pulse, and are combined with transfer efficiencies in a two-dimensional plot (**Figure S3**). For comparison, the dependences for a fixed distance (straight line) and a dynamic distance distribution (curved line) are displayed: the curves corresponding to the Gaussian chain and to the SAW distributions are overlaying.

End-to-end and intrachain distances (**Figure 2 e-f**) are recovered by rescaling the measured inter-dye distances by a factor $(N/(N+1))^{\nu}$, where N is the number of bonds in the segment of interest, $\nu = 9$

represents additional bonds that account for the dye linkers¹³, and ν is the scaling exponent associated with the Gaussian chain or the SAW distributions: $\nu_{Gauss} = 0.5$ and $\nu_{SAW} = 0.588$ ¹². An estimate of the radius of gyration (**Figure 2 g-h**) can then be obtained by dividing the average end-to-end distance values by the square root of the corresponding universal ratio, *i.e.*, $\sqrt{6}$ for the Gaussian chain and $\sim\sqrt{6.26}$ for the SAW¹². To extract scaling exponents, ν , for each denaturant concentration, for both R17 and ACTR we fit the inter-dye distances of the three variants in both denaturants to the scaling law:

$$R_{ij} = B|i - j|^\nu, \quad (S4)$$

where $B = 0.55 \text{ nm}^{14}$, $|i - j|$ corresponds to the number of peptide bonds in the segment probed by the dyes, and ν is a fitting parameter.

2f-FCS measurements.

2fFCS measurements of donor-labeled R17d 116 (“R17d-488”) were performed at 22 °C on a Micro Time 200 confocal microscope equipped with a differential interference contrast prism. The donor dye Alexa 488 was excited alternately with two orthogonally polarized diode lasers at 483 nm (LDH-D-C-485, PicoQuant), with a combined repetition rate of 40 MHz and power of 10 μW per laser at the sample. For measurements of acceptor-labeled ACTR, the acceptor dye Alexa 594 was excited alternately with two orthogonally polarized laser beams: one beam with wavelength $582 \pm 15 \text{ nm}$, selected with a z582/15 band pass filter (Chroma) from the emission of a SC-450-4 supercontinuum fiber laser (Fianium, UK) driven at 20 MHz, triggers (interleaved) pulses from a second supercontinuum laser with wavelength-selected output at $585 \pm 5 \text{ nm}$ (Solea, PicoQuant, Germany), with a combined repetition rate of 40 MHz and a power of 15 μW per laser at the sample.

The distance between the two foci δ was determined using three standards using an excitation wavelength λ_{ex} 485 nm and 585 nm: Alexa Fluor 488-labeled CspTmC67 (Csp-A488), hCypV2C (Cyp-A488), and monomeric GroEL-single ring (SR1-A488) or the corresponding Alexa Fluor 594-labeled proteins Csp-A594, Cyp-A594 and SR1-A594, all in 5.07 M GdmCl, 50 mM sodium phosphate, 100 mM β -mercaptoethanol, 0.001% Tween 20, pH 7.25¹⁴. The reference R_h values of the labeled proteins were determined under identical conditions using dynamic light scattering (DLS) with a Mambo-Laser 594nm (Cobolt, Sweden) at 100mW¹⁴. The focal distance δ was determined using the DLS R_h values as described in (14). The average of the fits from 4 independent calibrations yielded a δ of $447 \pm 2 \text{ nm}$ at $\lambda_{ex} = 485 \text{ nm}$ and 10 μW excitation power, and $473 \pm 2 \text{ nm}$ at $\lambda_{ex} = 585 \text{ nm}$ and 15 μW excitation power. Residual fluorescence background in the denaturant solution led to an increase in the apparent diffusion coefficient D of the sample. Thus, we measured free Alexa 488 dye at the same denaturant concentrations in which R17d-488 had been measured, and estimated a decrease of 0.3 to 5% in the calculated R_h between 0.2 and 7.3 M GdmCl, respectively, from the average of three independent experiments. This correction was used to calculate the upper error bounds of the 2f-FCS data reported in **Figure 4a**; urea exhibits similar average background to GdmCl, so we applied the same correction to the data in **Figure 4c**. ACTR displays a smaller change in R_h than R17d, so in this case we eliminated the

background contribution by using Alexa 594 excitation of suitably singly labeled sample (“ACTR-594”, **Figure 4b** and **d**). The concentration of labeled protein was between 1 and 6 nM in 50 mM sodium phosphate buffer, pH 7.0, in the presence of 140 mM β -mercaptoethanol and 0.01% Tween 20 with varying concentrations of GdmCl (Pierce) or urea (Sigma). The denaturant concentration of all samples was calculated from the refractive index, measured with an Abbe refractometer.

Ensemble fluorescence measurements

Equilibrium ensemble denaturation measurements were performed for R17d to assess its stability and ability to fold (**Figure S2**). Experiments were performed in 50 mM sodium phosphate with and without 1 M sodium sulfate with GdmCl as a denaturant on a Jobin-Yvon FluoroLog, monitoring intrinsic tryptophan fluorescence as described previously¹⁵. Data were analyzed assuming a two-state transition¹⁶ as in¹⁷.

Dynamic light scattering (DLS) experiments

Experimental set-up and data treatment

DLS experiments were done with an instrument which simultaneously measures static (SLS) and dynamic light scattering at a scattering angle of 90°. The custom-built apparatus is equipped with a diode-pumped continuous wave laser (Cobolt Samba 532 nm, 500 mW, Cobolt AB, Sweden), a high quantum yield avalanche photodiode and two photon correlators (ALV 7002E, laboratory-made correlator). The data acquisition system accumulates average scattering intensities and second order intensity time-autocorrelation functions (acf) $g^2(\tau)$ obtained for many short time-intervals (typically 10 s). The delay time τ ranges from 0.1 μ s to 0.1 s for estimating size distributions in terms of hydrodynamic radii, R_h , from 0.1 nm to several micrometers. Accumulated intensities and correlation functions for the individual intervals are visually inspected, and undistorted parts are averaged for further calculations. This type of data acquisition is important to eliminate the influence of residual aggregates, dust or other larger particles as much as possible. Original recordings of short-time averaged intensities are shown in **Figure S9c**, allowing us to analyze and to compare the initial solution quality of different protein samples. All measurements were done in Micro-fluorescence cells (Hellma Analytics, Germany, path length = 3 mm, V = 45 μ l).

Translational diffusion coefficients, D , were obtained from the measured autocorrelation functions using the program CONTIN¹⁸. CONTIN yields intensity distribution functions, $I(D)$, which can be calculated without further assumptions concerning the morphology of the particles. Diffusion coefficients are converted into Stokes radii via the Stokes-Einstein equation $R_h = k_B T / (6\pi\eta D)$, where k_B is Boltzmann’s constant, T is the temperature in Kelvin, and η is the solvent viscosity. Viscosities were measured using an Ubbelohde-type viscometer (Viscobot-2, Lauda, Germany). During the present experiments, precise viscosities were particularly important to minimize their contribution to the uncertainty of the calculated R_h .

Several aspects of the present DLS experiments took the method to its limits: the small changes in R_h (experimental error in DLS is about 2-3%), the presence of high concentrations of denaturant, leading

to strong solvent scattering, and the presence of further scattering particles due to unavoidable impurities. An additional and important task of the DLS experiments was to estimate the amount of aggregated protein, which could potentially influence the SAXS experiments, performed with identical samples. Therefore, we first performed measurements of untreated samples (i.e. defrosted samples dialyzed in different denaturant concentrations in Zurich, flash frozen and shipped to our lab on dry ice), then measured an equivalent aliquot after 15 min centrifugation at 12000 g, and finally measured a third aliquot of the same sample after ultracentrifugation at 75000 g for 30 minutes. “Untreated” samples, where the presence of aggregates was quantified for estimating a possible influence on SAXS measurements, were measured only once temperature equilibration (at 22 °C) was complete and within 30 minutes after defrosting; the same protocol was used for the SAXS experiments.

Figure S9c shows a 30-minute recording of scattering intensities of a solution of ACTR in 0.32 M GdmCl. For each 10-s interval, a corresponding autocorrelation function is calculated, allowing a short-time estimation of particle sizes. Some of the time-intervals are disturbed by small numbers of very large particles crossing the scattering volume, but enough data intervals can be accumulated in order to calculate more precise size distributions, as shown in **Figure S9d**. Weight or molar concentrations of different size classes can only be determined if the morphology of the particles and their specific scattering intensity is known. In the present case, the scattering of larger particles is comparable with that of the monomeric protein, therefore, considering that the size of such particles is on average 50-100 times larger than the monomeric protein, the weight concentration is estimated to be less than 1-2% of the total protein. Moreover, as shown in **Figure S9c**, centrifugation at 12000 g for 15 minutes reduced the number of aggregates appreciably (blue points), which is reflected in the reduction of width and height of the peaks around 50 nm (**Figure S9d**). Ultracentrifugation at 75000 g for 30 min almost completely removes large particles. Note that centrifugation at 21000 g for 10 minutes is a step in the sample preparation protocol for SAXS experiments, so the already tiny amount of slow-diffusing particles present in thawed samples was further reduced before SAXS measurements. We also compared protein concentrations of samples before and after ultracentrifugation; the results showed that the protein loss in % weight was within the uncertainty of the spectrophotometric measurements, i.e. $\leq 1\%$, suggesting that at least some of the larger particles detected could be non-proteinaceous sample impurities. Dilution of samples from high to low concentration of denaturant prior to measurement provided comparable results to the centrifugation protocol described above.

Protein concentration dependence of R_h

Solution nonideality must be taken into account at the protein concentrations used in DLS studies, resulting in a concentration dependence of D , usually approximated in the form $D(c) = D(0) \cdot (1 + k_D \cdot c)$ ¹⁹. k_D , the diffusive concentration dependence coefficient which can be used to characterize intermolecular interactions, can vary considerably in magnitude and sign and in dependence on solvent, conformational state, and net charge of the protein. Our measurements highlighted a weak protein concentration dependence of D (**Figure S9a**), resulting in a slight increase of the measured R_h with increasing protein concentration at low denaturant concentrations and a decrease of similar magnitude at

high denaturant concentrations (**Figure S9b**). To measure R_h values as accurately as possible, we used protein samples at the lowest useful concentration. R17d was measured between 0.14 and 5 mg/ml from 0.2 to 7.05 M GdmCl, and at 1.6 mg/ml between 0.62 M and 9.02 M urea (**Figure 4a** and **c**). ACTR was measured between 1.5 and 7.35 mg/ml between 0 and 6.94 M GdmCl and between 1.5 and 3.7 mg/ml between 0 and 8.96 M urea (**Figure 4b** and **d**). The results of the protein concentration dependence of D as a function of denaturant concentration imply that the R_h shown in **Figure 4a, b** and **c** is a slight overestimate or underestimate at low and high denaturant concentrations, respectively, which could be the reason why the expansion monitored with DLS seems to plateau earlier than *e.g.* 2f-FCS experiments. Enough data could be collected for ACTR between 0 to 8.96 M urea to extrapolate to infinite protein dilution (**Figure 4d**), which resulted in very similar values of R_h as the lowest protein concentrations.

Ensemble refinement

Explicit ensembles of structures were generated using the implicit-solvent model ABSINTH²⁰, with the CAMPARI program, with the OPLS version of the model, and using a temperature-independent implicit solvent. While a temperature-dependent implicit solvent has been described²¹, in this case our aim was to generate a range of samples with different radius of gyration, by varying the temperature. To this end, temperature replica exchange Monte Carlo was run for 1.3 million steps, spanning a range of 280 to 2446 K with 64 replicas, starting from a fully extended configuration. At each temperature, the first 0.3 million steps were for equilibration, and 10,000 protein configurations were evenly recorded in the productive run. These configurations were fitted to the experimental data using the EROS procedure²², with the following target function:

$$G(\{w_i\}) = 0.5\chi^2 - T_{\text{fit}}S(\{w_i\})$$

In this equation, $0.5\chi^2$ is the negative log likelihood of observing the experimental data given the ensembles, if we model the error as a Gaussian function (multivariate Gaussian for correlated data set like SAXS intensity). χ^2 is also the conventional un-normalized chi-square function expressing the agreement between the FRET and SAXS experimental data and the results back calculated from the model, when a set of normalized weights $\{w_i\}$ is assigned to the structures in the ensemble, *i.e.*

$$\chi^2 = \sum_{r \in \text{FRET}} \frac{(E_r^{\text{sim}}(\{w_i\}) - E_r^{\text{expt}})^2}{(\sigma_r^{\text{expt}})^2} + [\mathbf{I}^{\text{sim}}\{w_i\} - \langle \mathbf{I}^{\text{expt}} \rangle]^T \mathbf{M} \Sigma^{-1} [\mathbf{I}^{\text{sim}}\{w_i\} - \langle \mathbf{I}^{\text{expt}} \rangle]$$

In this expression, $E_r^{\text{sim}}(\{w_i\})$ are the FRET efficiencies and $\mathbf{I}^{\text{sim}}\{w_i\}$ is the vector of SAXS scattering intensities (indexed by q) back-calculated from the ensemble, given the set of weights $\{w_i\}$, E_r^{expt} and $\langle \mathbf{I}^{\text{expt}} \rangle$ are the corresponding experimental quantities, and σ_r^{expt} the experimental errors from FRET. The matrix Σ^{-1} is the pseudo-inverse of the covariance matrix Σ of a set of M independent measurements of SAXS intensities, \mathbf{I}^{expt} , whose average is $\langle \mathbf{I}^{\text{expt}} \rangle$. In addition to χ^2 , the second term $T_{\text{fit}}S(\{w_i\})$ is added to prevent overfitting, where $S(w_i) = -\sum_i w_i \ln w_i$ is the Shannon entropy and the “temperature” T_{fit} is a variable to control how strongly the weights are biased to be equal, expressing the prior that the reweighted ensemble should differ minimally from the original one. The optimization consisted of performing simulated annealing of the $\{w_i\}$ in order to minimize G . The parameter T_{fit} was chosen to be

the highest at which a good fit was still obtained, obtained from the point at which χ^2 begins to sharply increase in a plot of χ^2 versus S (**Figure S10**). Errors were estimated by Metropolis Monte Carlo sampling of the posterior distribution of weight sets $\{w_i\}$, in which G is used as the energy at unit temperature.

SI Tables

R17 SAXS/DLS (“R17d”)	¹ GS RLEES ⁶ L EYQQFVANVEEEEEAWINEKMTLVASEDYGD ³⁹ T L A AIQGLLKKHEAFETDFTV HKDRVNDV A ANGEDLIKNNHHVENITAKMK G A KGKVS D L E K AAAQRKAKLDENSAFL Q ₆₆ ₉₀ ₉₉ ₁₁₆
R17d 1-116 (FRET)	GS C LEESLEYQQFVANVEEEEEAWINEKMTLVASEDYGD ³⁹ T L A AIQGLLKKHEAFETDFTV HKDRVNDV A ANGEDLIKNNHHVENITAKMK G A KGKVS D L E K AAAQRKAKLDENSAFL C
R17 6-99 (FRET)	GS RLEES C EYQQFVANVEEEEEAWINEKMTLVASEDYGD ³⁹ T L A AIQGLLKKHEAFETDFTV HKDRVNDV A ANGEDLIKNNHHVENITAKMK G L G KGVSD L E C AAAQRKAKLDENSAFL Q
R17 39-99 (FRET)	GS RLEESLEYQQFVANVEEEEEAWINEKMTLVASEDYGD ³⁹ T L C AIQGLLKKHEAFETDFTV HKDRVNDV A ANGEDLIKNNHHVENITAKMK G L G KGVSD L E C AAAQRKAKLDENSAFL Q
ACTR SAXS/DLS	¹ GP S GTQNRPLLRNSLDDLVGPPSNLEGQSDER ³¹ A LLDQLHTLLSNTDATGLEEIDRALGI P ELVNQGQALEPKQ D S GGPR ₅₉ ₇₃
ACTR 1-73 (FRET)	GP C GTQNRPLLRNSLDDLVGPPSNLEGQSDERALLDQLHTLLSNTDATGLEEIDRALGI P ELVNQGQALEPKQ D C
ACTR 1-59 (FRET)	GP C GTQNRPLLRNSLDDLVGPPSNLEGQSDERALLDQLHTLLSNTDATGLEEIDRALGI P C LVNQGQALEPKQ D S
ACTR 31-73 (FRET)	GP SGTQNRPLLRNSLDDLVGPPSNLEGQSDER C LLDQLHTLLSNTDATGLEEIDRALGI P ELVNQGQALEPKQ D C

Table S1. Amino acid sequences of R17 and ACTR variants used in the present investigation. In R17 SAXS/DLS and ACTR SAXS/DLS, all positions which have been mutated in the FRET variants are bold and labeled with their respective number, while the cyan shading indicates R17 residues which have been mutated with respect to the wt protein, as explained in the SI (Choice of protein variants). Bold, yellow-shaded Cys residues represent positions where the dyes were attached. Red-colored residues were part of protease recognition sites used to cleave the HisTag and avi-tag with HRV-3C (GP) and thrombin (GGPR and GS), respectively. Note that the wt sequence of ACTR extends between residues 2 and 72⁴, with the two serine residues added at both termini to afford FRET measurements of the full-length wt sequence.

Measurement	ACTR in Urea	*ACTR in Urea	ACTR in GdmCl	R17d in Urea	R17d in GdmCl
	0.58 M : 8.96 M	1.04 M : 9.01 M	0.32 M : 6.95 M	0.62 M : 9.02 M	0.58 M : 6.93 M
R	1.28	1.48	1.32	1.43	1.33
R_g	1.22	1.24	1.20	1.30	1.22
R_h	1.09	1.10	1.09	1.14	1.10

Table S2: Relative changes (value at higher denaturant concentration divided by that at the lower concentration) in R , R_g , R_h obtained from structural ensembles for R17d and ACTR in GdmCl and Urea, fitted to FRET and SAXS data. * indicates the same observation from all-atom molecular dynamics simulations, although at slightly different denaturant concentrations.

ACTR	Hydrophilic* dye pairs		Hydrophobic* dye pairs	
	Alexa 488/ Alexa 594	Atto 532/ CF 640R	Atto 532/ Abberior STAR 635	Atto 532/ Atto 647N
R_0 (buffer) (nm)	5.4	5.9	6.0	6.1
R_0 (5.6 M GdmCl) (nm)	5.2	5.6	5.7	5.8
E (buffer)	0.59	0.68	0.86	0.89
E (5.6 M GdmCl)	0.48	0.59	0.61	0.60

Table S3: Förster radii R_0 and transfer efficiencies measured for ACTR doubly labelled with hydrophilic or hydrophobic donor-acceptor dye pairs in buffer and 5.6 M GdmCl. It is evident that the two measurements performed with hydrophilic dye pairs return transfer efficiencies of comparable value, which is much lower than those obtained for the same protein labelled with more hydrophobic dyes. *Hydrophobicity ranking: CF 640R < Alexa 488 < Atto 532 < Alexa 594 < Abberior STAR 635 < Atto 647N (from reverse-phase HPLC results reported in **Figure S15**; information on dye manufacturers are given in **Figure S15** caption).

Fitting input	Hydrophilic dye pair: Alexa 488 / Alexa 594		Hydrophobic dye pair: Atto 532 / Abberior STAR 635	
	χ^2	R_g (nm)	χ^2	R_g (nm)
FRET only	6.32	2.41 ± 0.06	177.2	1.63 ± 0.05
SAXS only	3.89	2.51 ± 0.03	273.2	2.51 ± 0.03
FRET and SAXS	0.81 ($T_{fit} = 20$)	2.48 ± 0.02	0.82 ($T_{fit} = 1$)	2.50 ± 0.04

Table S4: Example for ensemble refinement results using the hydrophobic dye Abberior Star 635 as an acceptor for FRET in ACTR to illustrate the sensitivity of the ensemble analysis for inconsistent data (see main text for discussion). The corresponding transfer efficiency measured for these dye pairs are in **Table S3**; for dyes hydrophobicities from RP-HPLC see **Figure S15** and caption of **Table S3**. The reference (Alexa 488/Alexa 594) is for ACTR in 0.32M GdmCl, the data with Atto 532/Abberior Star 635 in water. When fitting only to FRET data, χ^2 from SAXS is provided, and vice versa.

Protein/Denaturant	*FRET SAW	*FRET Gaussian	*SAXS	*Ensemble	#Ensemble FRET	#Ensemble SAXS
[Denaturant] \geq 0M						
R17d/GdmCl	-171.0	-174.5	-19.5	-62.7	-38.9	-38.8
R17d/Urea	-173.9	-176.1	-145.5	-163.3	-58.8	-69.6
ACTR/GdmCl	-156.4	-173.9	-69.1	-206.5	-55.8	-113.0
ACTR/Urea	-97.5	-100.5	-23.4	-140.3	-21.0	-85.7
[Denaturant] \geq 3M						
R17d/GdmCl	-2.3	-2.5	1.1	-5.6	1.1	-1.4
R17d/Urea	-11.8	-12.2	0.8	-9.0	-7.0	-3.5
ACTR/GdmCl	-9.2	-11.1	-2.3	-3.2	-4.7	0.7
ACTR/Urea	-4.9	-5.2	1.1	-29.8	-2.8	-22.9

Table S5: Statistical test of the dependence of R_g on denaturant concentration. Two linear fitting models are used in the test, one with two free parameters (M_2), namely $R_g = a[\text{denaturant}] + b$ and one with one free parameter (M_1), i.e. $R_g = b$. The Bayesian information criterion (BIC)²³ defined as $BIC_M = \chi^2 + k_M \ln(n)$ is used to test the goodness of M_2 and M_1 in reproducing the experimental data, in which k_M is the number of free parameters in model M and n is the number of data points. $\chi^2 = \Sigma(R_{g,fit} - R_g)^2 / \sigma^2$ is the standard (non-reduced) χ^2 parameter. The BIC balances the improvement in χ^2 obtained with each additional free parameters with a corresponding penalty, thus providing a useful tool to select the best fitting model while avoiding the risk of overfitting: a smaller BIC score suggests a better model. The difference $\Delta BIC = BIC_{M_2} - BIC_{M_1}$ is reported either fitting to all the data we have or only to the data with denaturant concentration no smaller than 3M. A negative value of ΔBIC suggests that model M_2 is the better model, i.e. that R_g varies with denaturant concentration. The entries with $\Delta BIC \geq -2$ are highlighted in boldface, indicating that statistically we cannot determine if the chain expands with increasing denaturant in these cases. When using the data in all denaturant conditions, we unambiguously observe the chain expansion in all experimental measurements and computational models. When using data in only medium to high denaturant concentrations ($\geq 3M$), three of the four cases in SAXS fail to see statistically significant trend between R_g and denaturant concentrations, and in the fourth the ΔBIC still only provides weak support for a significant trend. This test shows that the number of data points and the magnitude of the errors relative to the change in R_g are critical to observe chain expansion when increasing denaturant concentrations. * corresponds to the data in **Figure 6** of the main text, and # the ensemble refinement R_g using one source of experimental measurement shown in **Figure S13**.

SI Figures

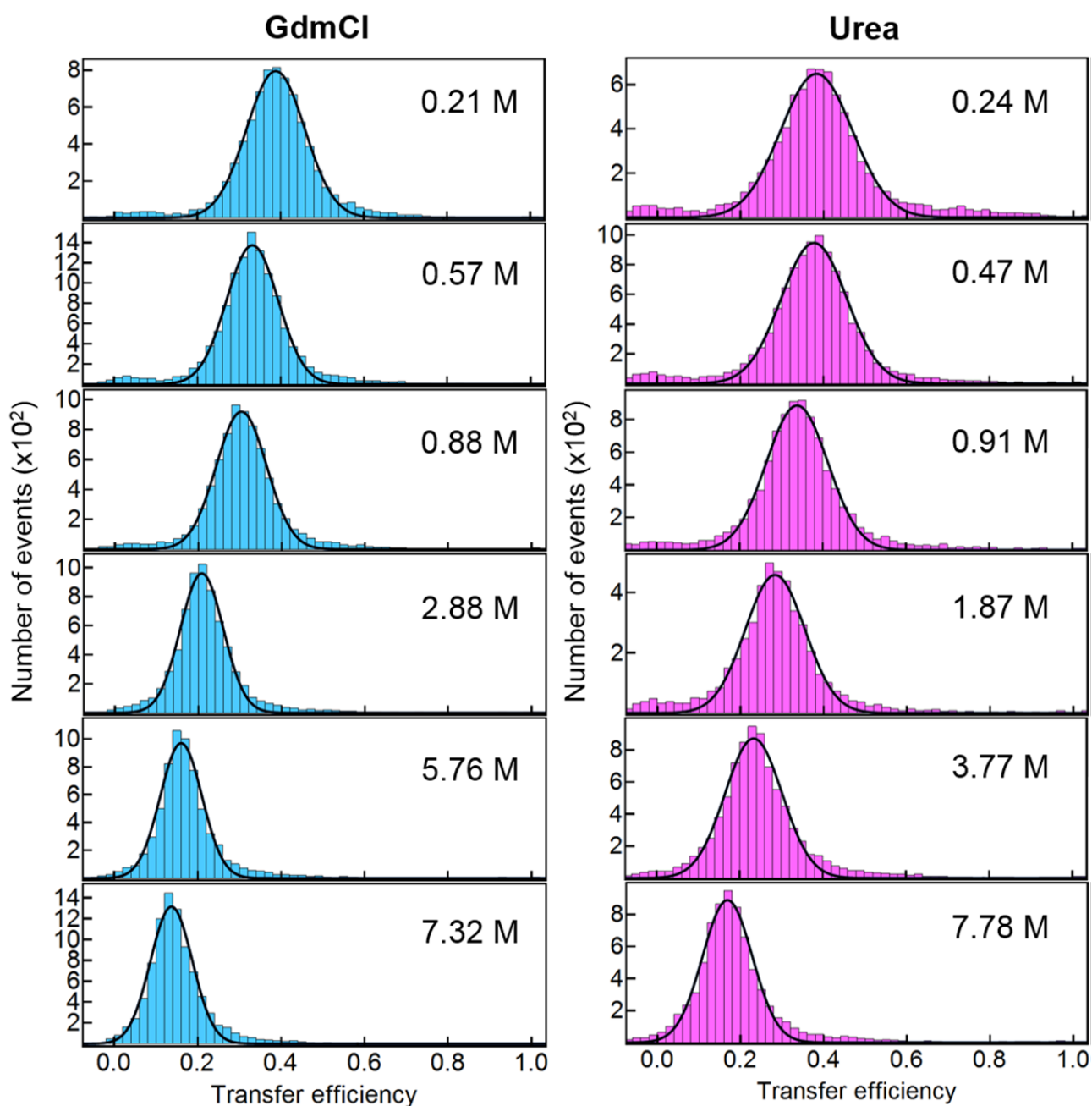


Figure S1. Single-molecule FRET efficiency histograms. Histograms of R17d 1-116 doubly labeled with Alexa 488 and 594 in 50 mM sodium phosphate buffer pH 7 at various concentrations of GdmCl (blue, left) and urea (magenta, right). A continuous decrease in the mean transfer efficiency indicates that the unfolded state expands with increasing concentration of both denaturants, and confirms that the native state is populated to an undetectable extent at all denaturant concentrations investigated (see also **Figure S2**).

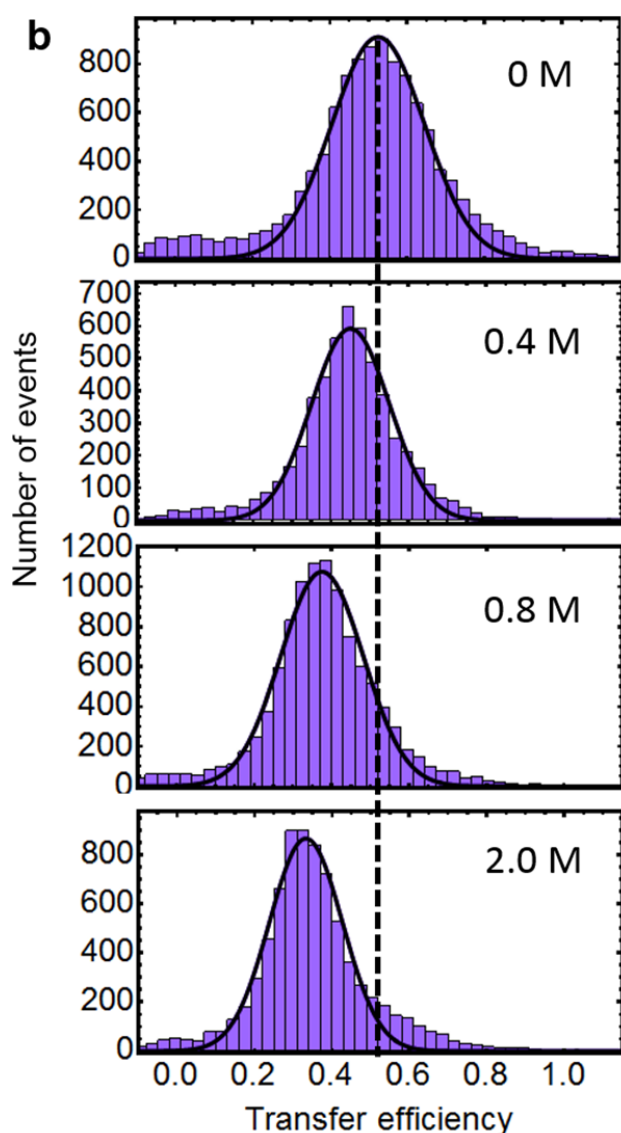
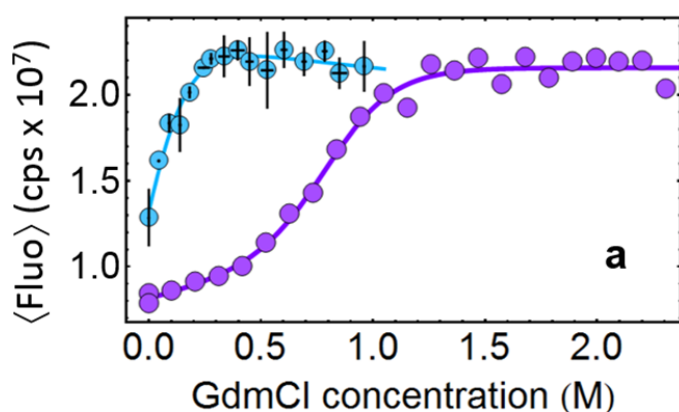


Figure S2. Equilibrium denaturation experiments of R17 C66A/L90A (R17d). **(a)** Ensemble denaturation curves of R17d (unlabeled protein used for SAXS and DLS): the Trp fluorescence emission intensity ($\langle \text{Fluo} \rangle$, in counts per second) averaged from 340 to 360 nm of the protein in sodium phosphate 50 mM pH 7 (blue circles) is plotted against GdmCl concentration. Given the lack of a native baseline, the narrow transition region, and the conservative nature of the two R17d mutations, data were fitted with the m -value fixed to the published value for R17 wt in GdmCl ($5.15 \text{ kcal} \cdot \text{mol}^{-1} \cdot \text{M}^{-1}$)²⁴ as described in ¹⁷. The resulting denaturation midpoint $D_{50\%}$ is $\sim 0 \text{ M}$ GdmCl, indicating that about half of the protein is unfolded in native buffer conditions, with the unfolding transition being complete at $\sim 0.2 \text{ M}$ GdmCl. The purple circles represent a denaturation curve of R17d in GdmCl in the same phosphate buffer plus 1 M sodium sulfate, which is known to stabilize this protein²⁵. A fit to the data without constraints yields an m -value of $\sim 3.8 \text{ kcal} \cdot \text{mol}^{-1} \cdot \text{M}^{-1}$, and a $D_{50\%}$ of $\sim 0.8 \text{ M}$ GdmCl. **(b)** Single-molecule FRET histograms of (doubly labeled) R17d 1-116 in 50 mM sodium phosphate in the presence of 0.5 M sodium sulfate. The presence of only one peak at every GdmCl concentration (given in each panel) and the continuous decrease of its transfer efficiency indicate that this is the only state populated by the doubly labelled protein in these stabilizing conditions, also suggesting that the singly labeled variant used in 2f-FCS experiments populates the folded state to a negligible extent in native buffer. The protein's

mean transfer efficiency in this solvent is always ~ 0.1 higher than in sodium phosphate 50 mM, which is consistent with ensemble equilibrium denaturation results reported in (a), showing a lower m -value for the unfolding transition, *i.e.* a more compact unfolded state^{26,27}.

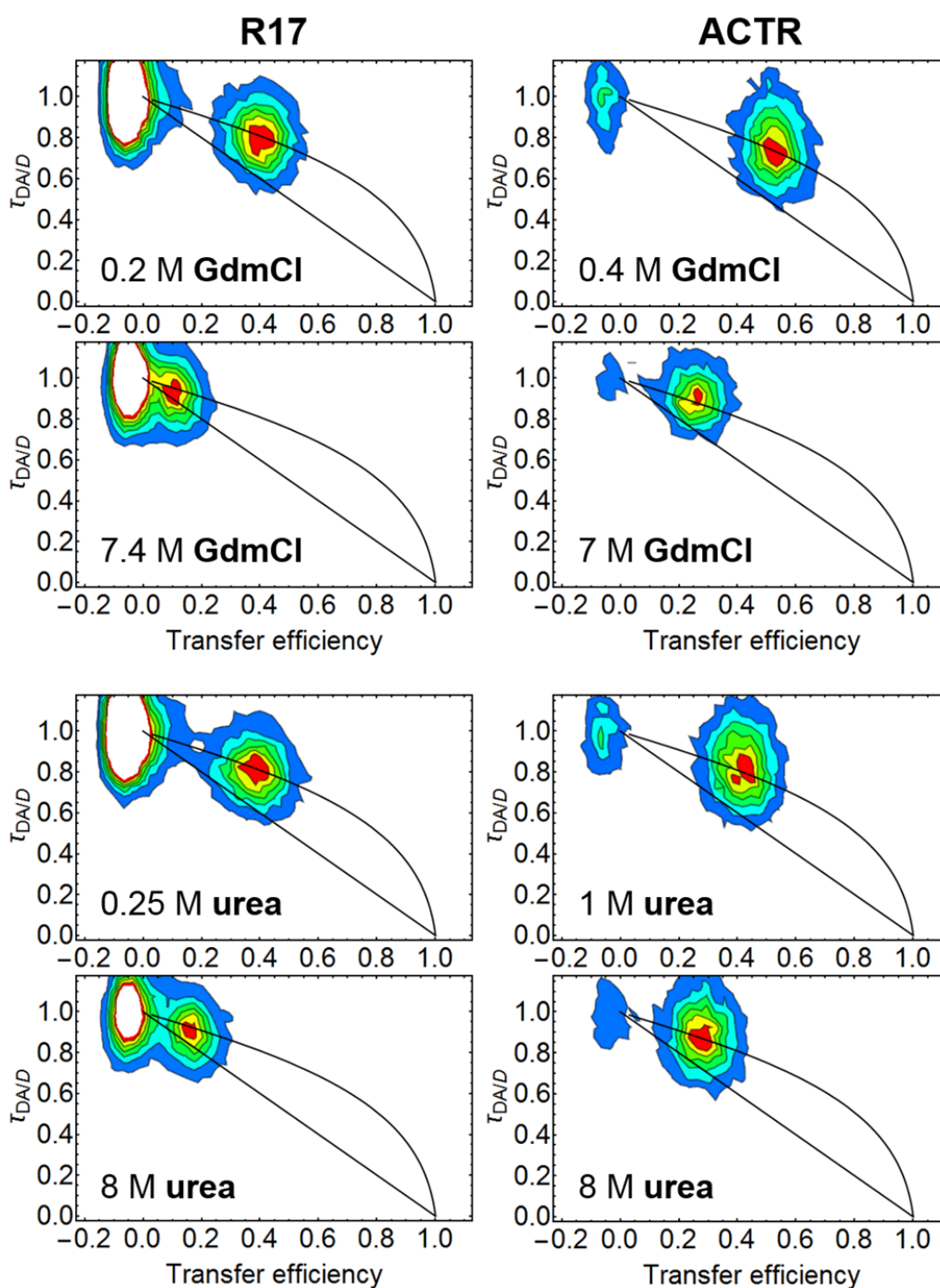


Figure S3. 2D-histograms of relative fluorescence lifetimes τ_{DA}/τ_D versus FRET efficiencies, E , for R17d 1-116 and ACTR 1-73 at low and high concentrations of GdmCl and urea. τ_{DA} and τ_D are the donor lifetimes in the presence and absence of the acceptor, respectively. The lines within the plots represent the expected dependences of lifetimes on transfer efficiencies for a chain where the inter-dye distance within the duration of a burst can be either considered fixed (straight lines) or averaged over the equilibrium distribution of distances for a Gaussian chain or SAW (yielding overlaying curves)²⁸.

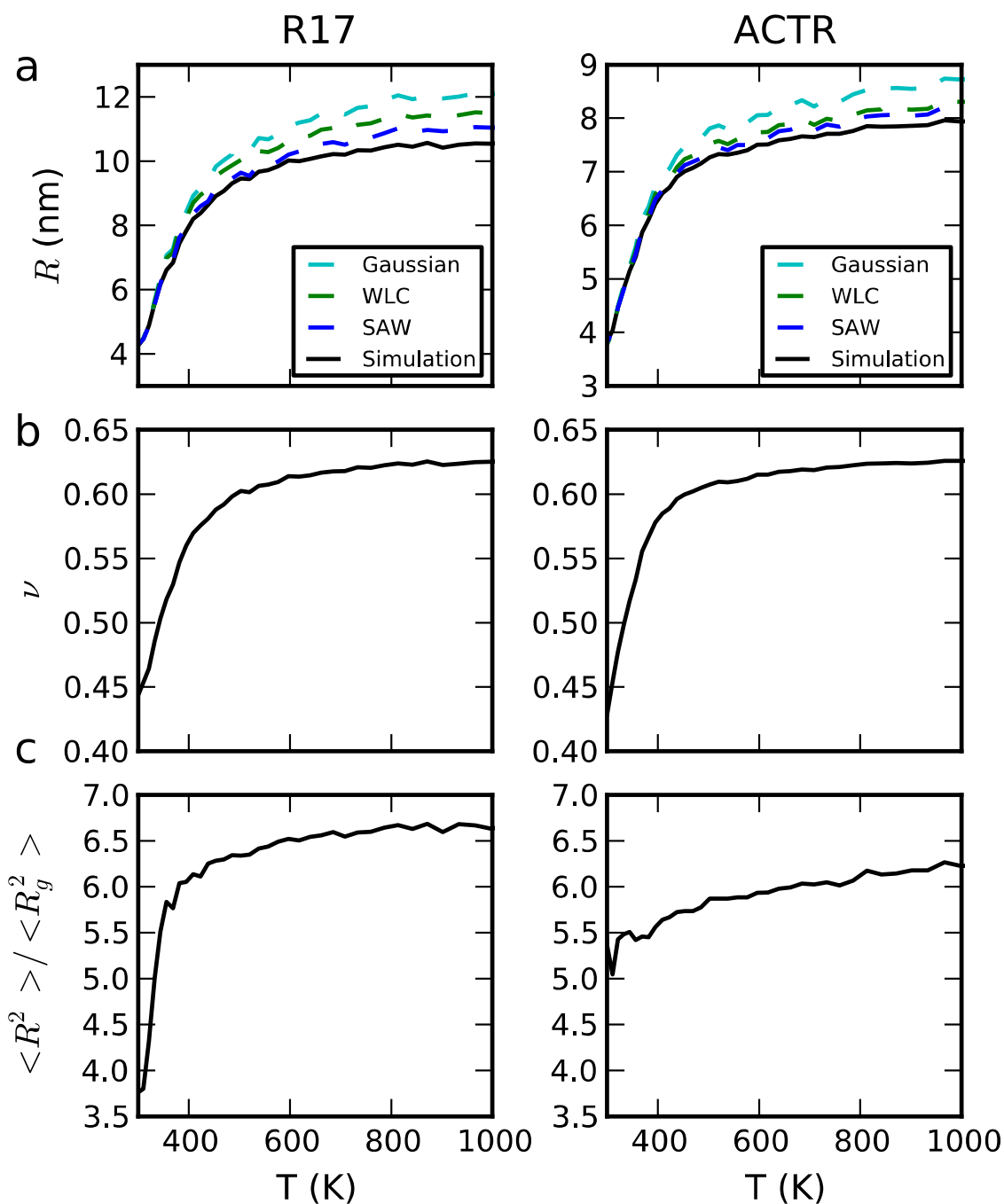


Figure S4. Investigation of polymer models for obtaining the end-to-end distance R from FRET efficiency using structure ensembles from a temperature replica exchange simulation with the ABSINTH simulation model²⁰ (without any reweighting using experimental information). **(a)** The end-to-end distance back-calculated from FRET efficiency obtained from true end-to-end distance in the ABSINTH simulation ensemble. In the legend, Gaussian is the Gaussian chain model, WLC the worm-like chain model, and SAW the self avoiding walk model. **(b)** The corresponding polymer scaling coefficient ν , using a prefactor B of 0.55 nm to fit the data set, according to Eq. S4. **(c)** The ratio between root-mean-squared end-to-end distance and root-mean-squared R_g .

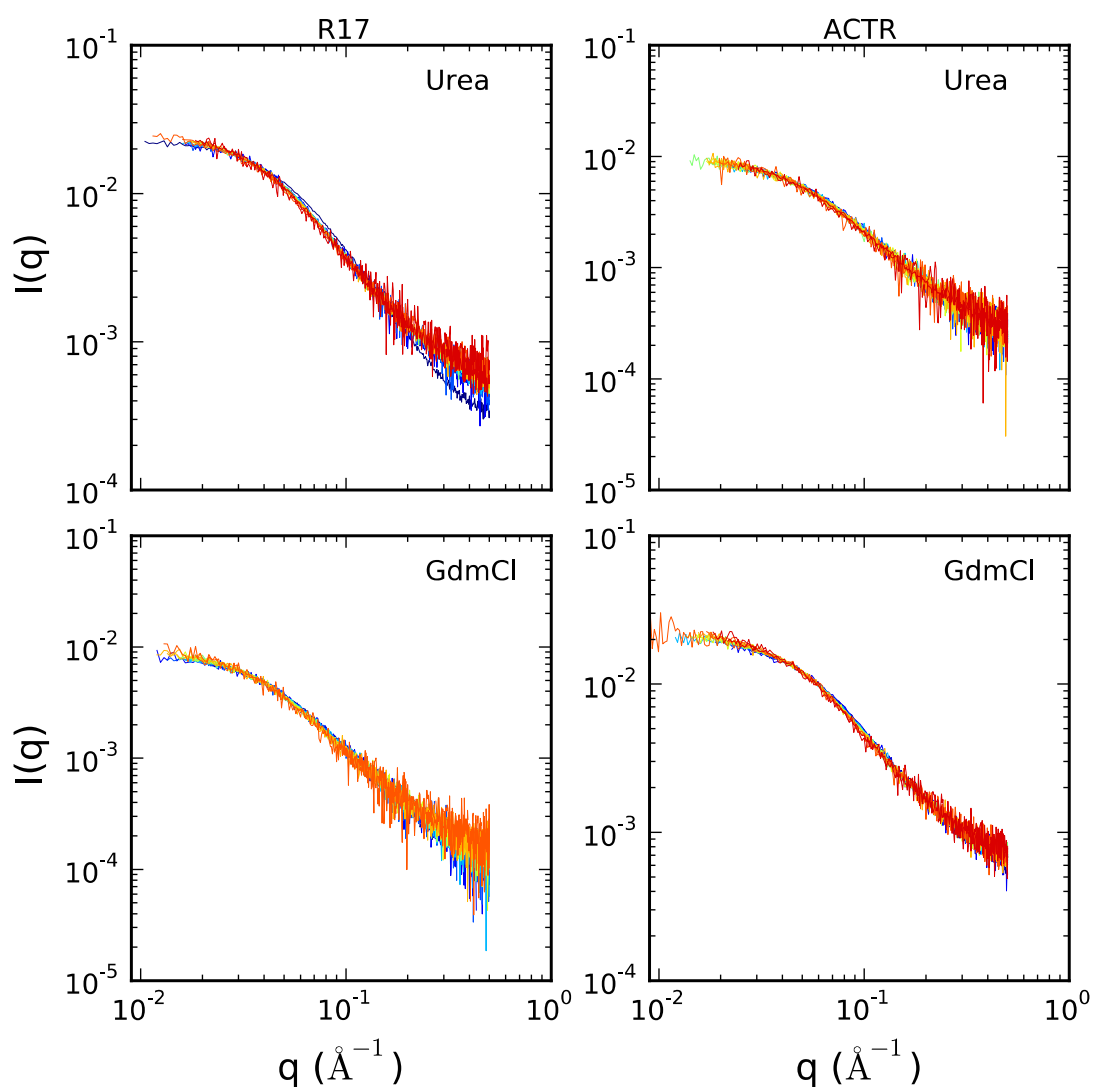


Figure S5. SAXS intensities $I(q)$ at all protein concentrations and denaturant concentrations. Color scheme of denaturant concentration is the same as labeled in **Figure S10**. $I(q)$ is superimposed to the $I(q)$ in the smallest denaturant concentration by both a scale and a shift for illustration.

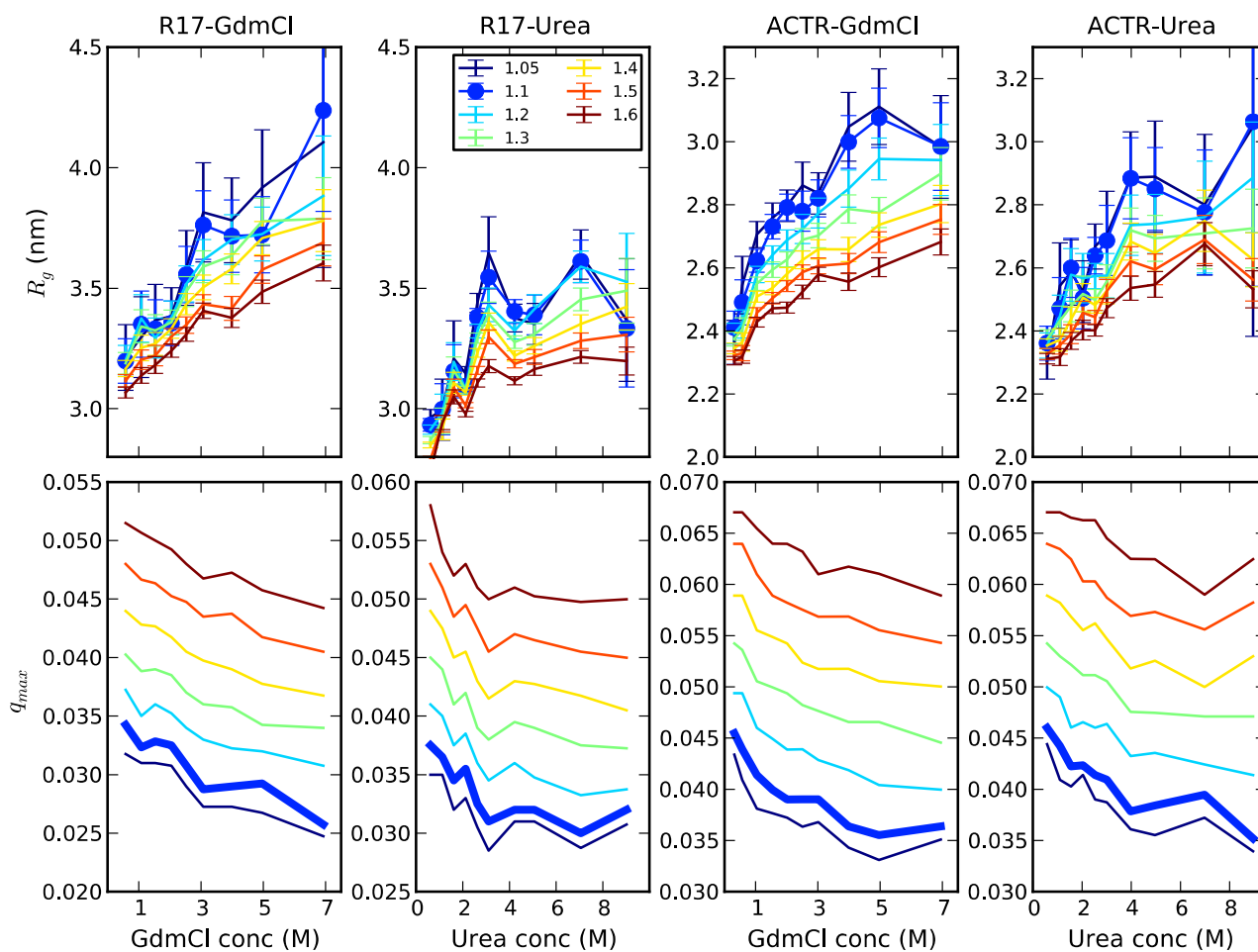


Figure S6. Guinier fits of SAXS measurements using different fitting ranges (see legend for color code of maximum $q_{max}R_g$ used in fitting). Symbols and thick lines show the R_g and the corresponding q_{max} reported in **Figure 6** of the main text.

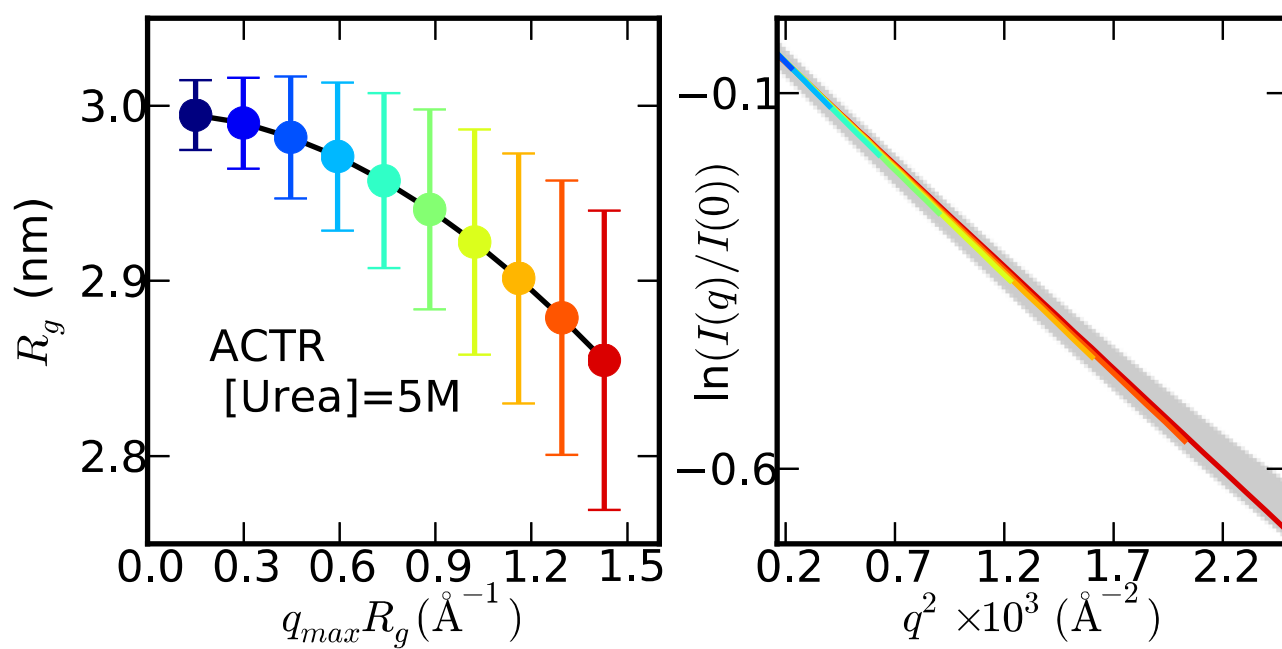


Figure S7. Guinier fits (right) from all-atom MD simulations of ACTR using different fit ranges converge to a constant R_g only in the limit $q_{max} \rightarrow 0$.

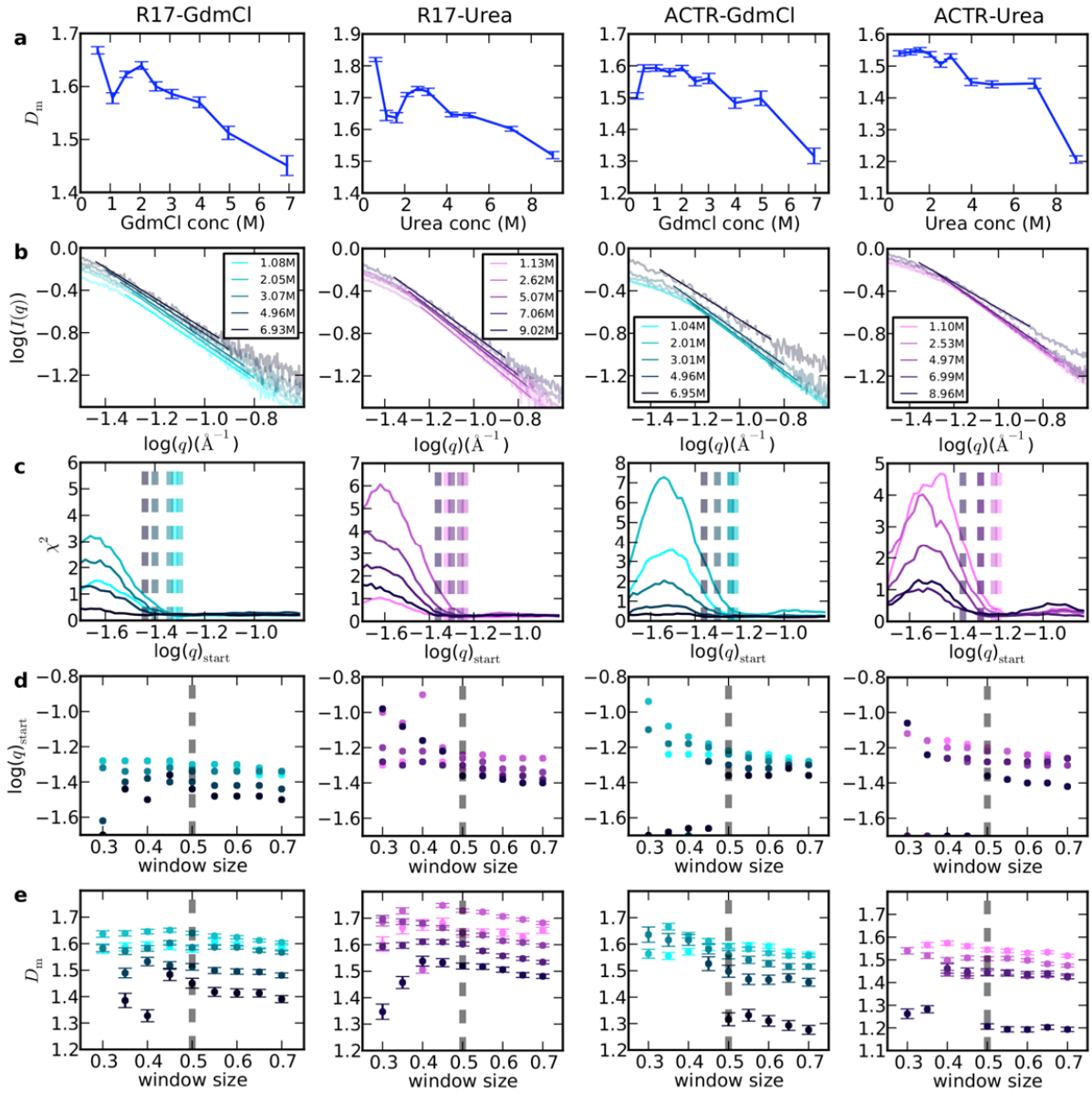


Figure S8. Mass fractal dimension D_m of R17d and ACTR from SAXS at intermediate q . The SAXS data in the high protein concentration is used because of the SAXS intensity errors at intermediate q for low protein concentration. **(a)** the mass fractal dimension. **(b)** The curve fitted to the experimental data using the range of q given the best linear fit. There are two parameters for determining the fitting range: the fitting window size on $\log(q)$ and the starting point of the fitting range, $\log(q)_{\text{start}}$. **(c)** The starting point of the fitting range is determined by monitoring the discrepancy χ^2 of the fitting and the smallest $\log(q)$ with χ^2 smaller than the mean χ^2 in the tail $\langle \chi(\log(q)_{\text{start}})^2 \rangle_{\log(q)_{\text{start}} \in [-1.0, -0.8]}$ for a specific fitting window size. **(d)** The starting point of the fitting range as a function of the window size. **(e)** The mass fractal dimension when varying window size. The corresponding starting fitting range and window size are shown as the dash lines. We find when the fitting window size is sufficiently large (>0.5), the mass fractal dimension value starts to converge, though there is a clear trend that higher denaturant data prefer a smaller starting point for the fitting range.

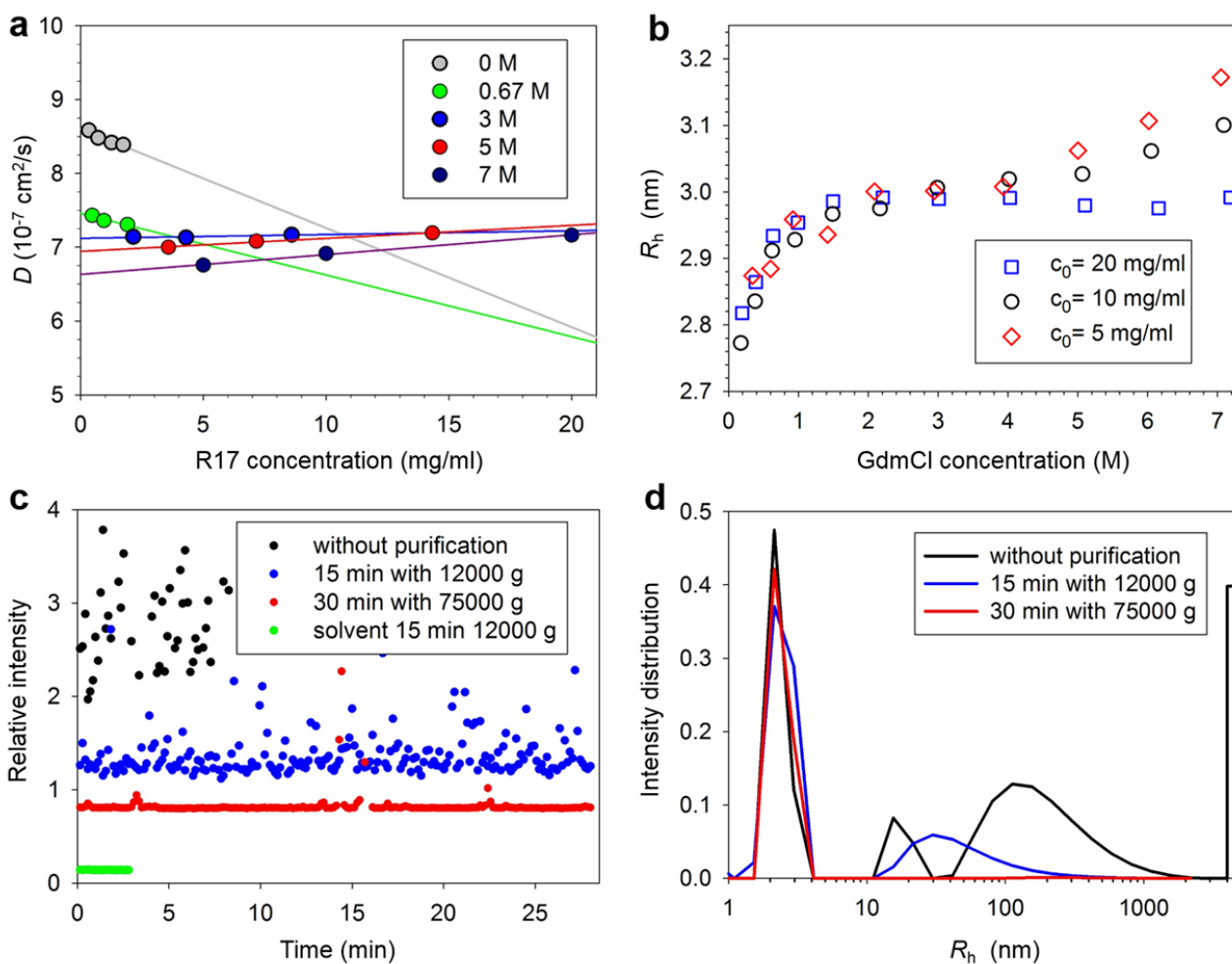


Figure S9. Concentration dependence of R17d diffusion coefficient D (a) and R_h (b) at selected GdmCl concentrations: at low denaturant concentrations, attractive interactions between protein molecules seem to exist, causing a slight decrease of D (*i.e.* larger apparent R_h) with increasing protein concentration, while at denaturant concentrations above $\sim 4 \text{ M}$ GdmCl, the protein-protein interactions seem to become repulsive, leading to a larger measured D (*i.e.* smaller apparent R_h) with increasing protein concentration; the red diamonds in (b) are the data shown in **Figure 4a** (only data above 0.2 M GdmCl are shown, where the contribution of folded R17d is negligible (see **Figure S2**)) (c). Example of a 30-minute recording of relative scattering intensities of a solution of 3.46 mg/ml of ACTR in 0.32 M GdmCl taken directly after thawing (black), after centrifugation at 12000 g (blue) and after ultracentrifugation (75000 g , red). For each 10-s interval, a corresponding autocorrelation function is calculated, allowing a short-time estimation of particle sizes. Some of the time intervals are disturbed by small numbers of very large particles crossing the scattering volume, but enough data intervals can be accumulated in order to calculate the size distributions shown in (d). The area below the curves in (d) (color coded as in (c)) in this figure is a measure of the scattering intensity of a particular size class, which is linked to the weight concentration in a non-trivial manner (see SI text); the bar on the right represents the scattering of all particles larger than the size range shown.

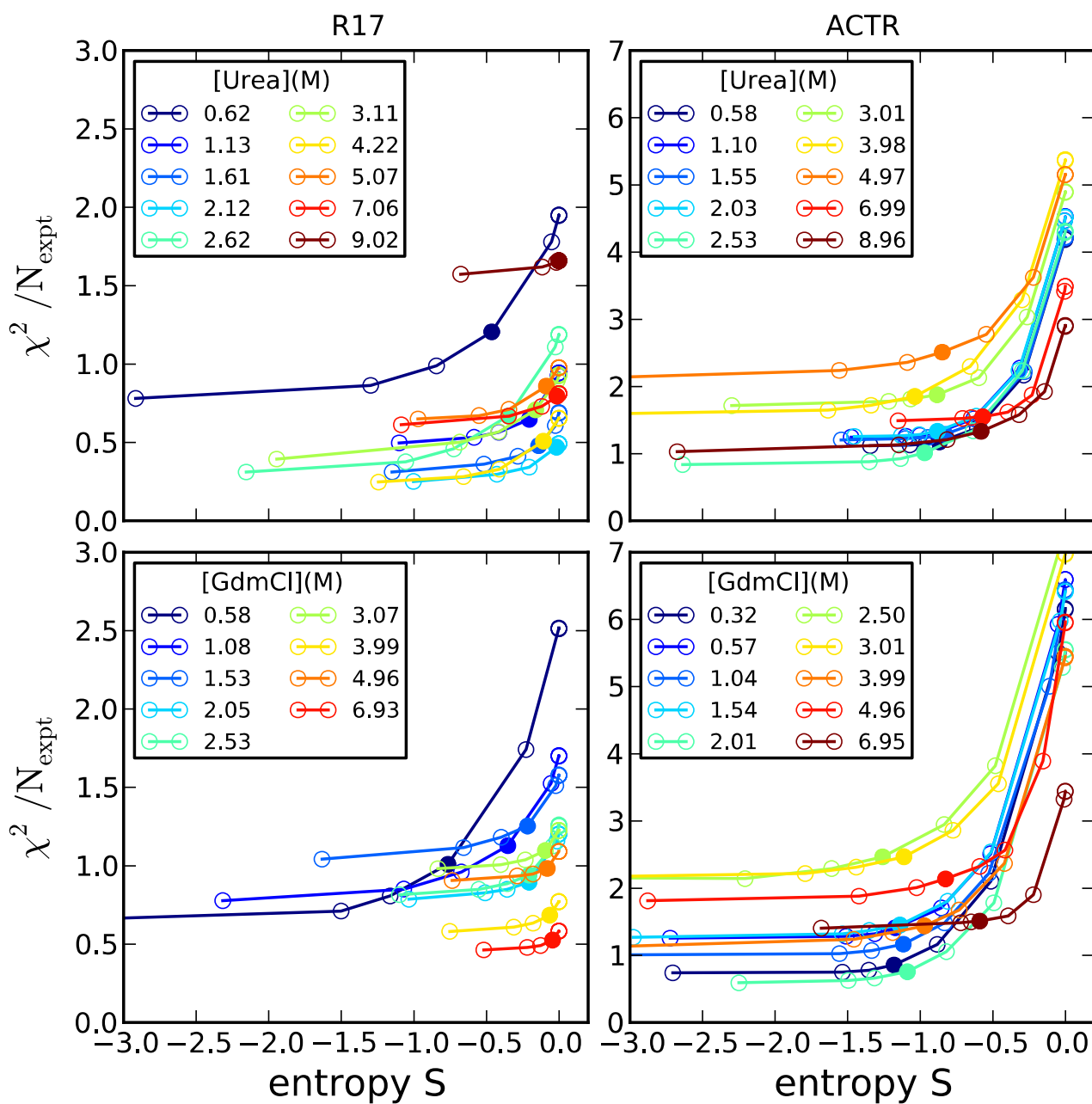


Figure S10. Entropy of ensemble reweighting analysis. N_{expt} is the number of independent experimental measurements used in the ensemble fit (30 measurements from SAXS and 3 from FRET for each protein at each denaturant concentration). Solid symbols show the entropy of the ensemble we report for each case.

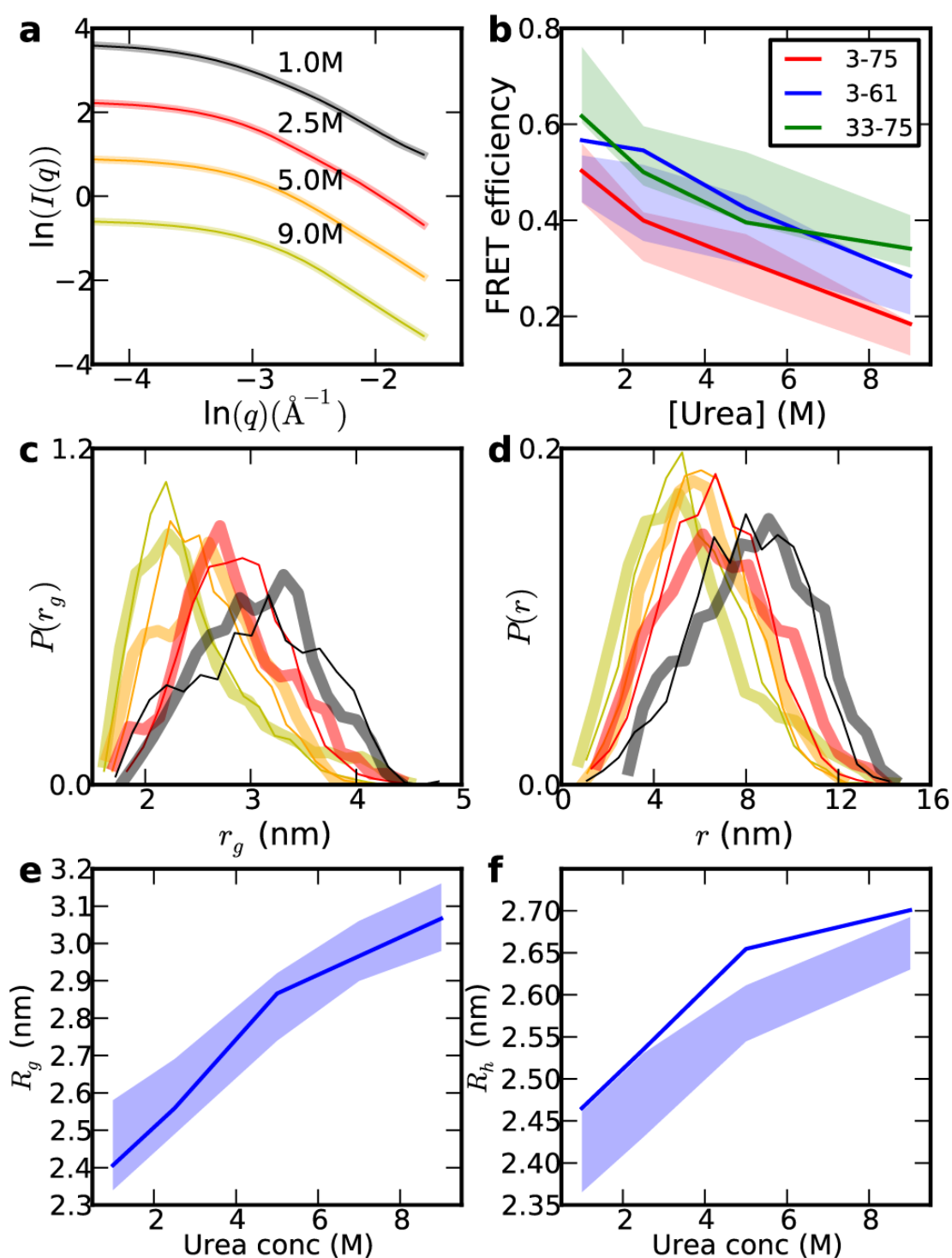


Figure S11. Recovery of the R_g distributions from all-atom simulations by using the “FRET” and “SAXS” data calculated from the all-atom model for our ensemble reweighting. The simulation data are taken from all-atom simulations of ACTR in urea from Ref.²⁹ **(a)** Fitting to all-atom “SAXS”; **(b)** Fitting to all-atom “FRET”; **(c)** and **(d)** distributions of r_g and r ; **(e)** R_g , and **(f)** R_h . The true distributions from the all-atom simulation are always shown with a thick line and the distributions recovered from ensemble reweighting with a thin line.

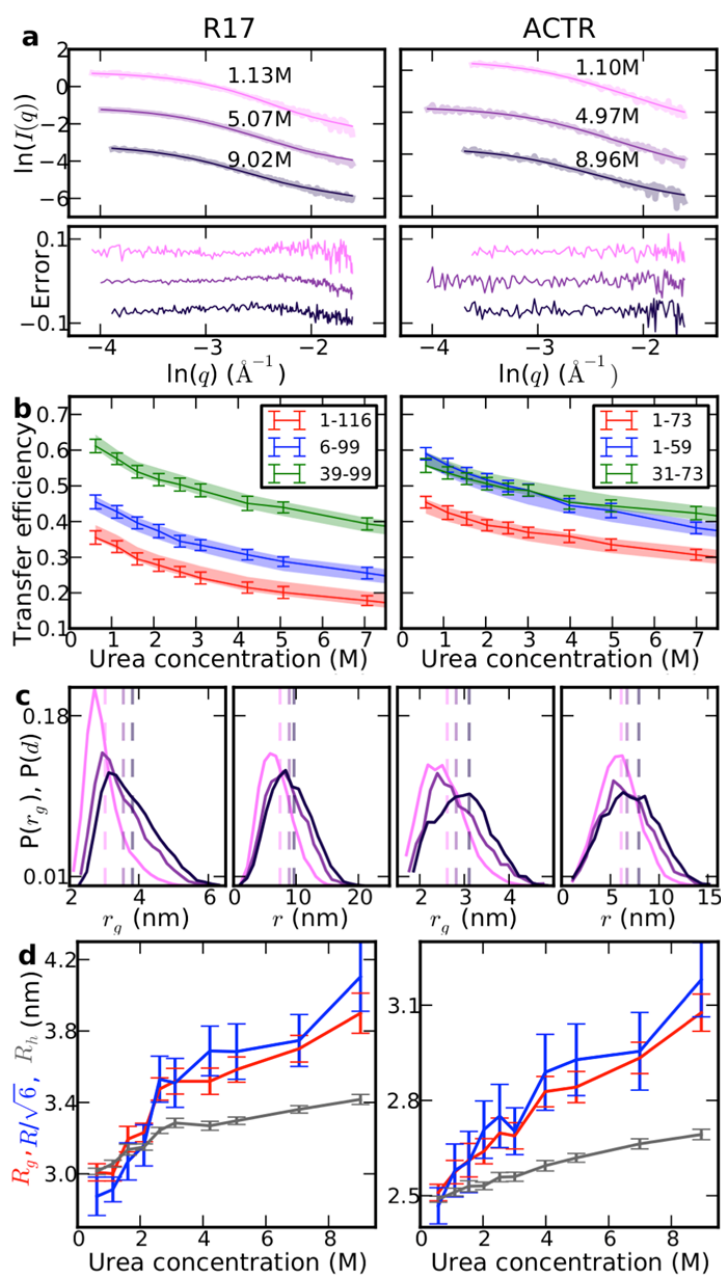


Figure S12. Results from refined ensembles using SAXS and FRET data of R17d (left) and ACTR (right) in urea. **(a)** Examples of calculated scattering curves from the ensemble model compared to SAXS data in urea and residuals (below). **(b)** FRET efficiencies calculated from the same models compared to experimental results for three different sets of labeling positions (see legend for label positions). Shaded bands represent experimental data (width of bands corresponding to systematic error). **(c)** Variation of r_g and end-to-end distance (r) distributions of ensembles for different denaturant concentrations (colors as labelled in (a)). The corresponding root-mean-squared end-to-end distances, R , are shown as vertical dashed lines. **(d)** R_g , R , and R_h from the reweighted ensembles as a function of GdmCl concentration. We plot $R/\sqrt{6}$ to place R on the same scale as R_g and R_h .

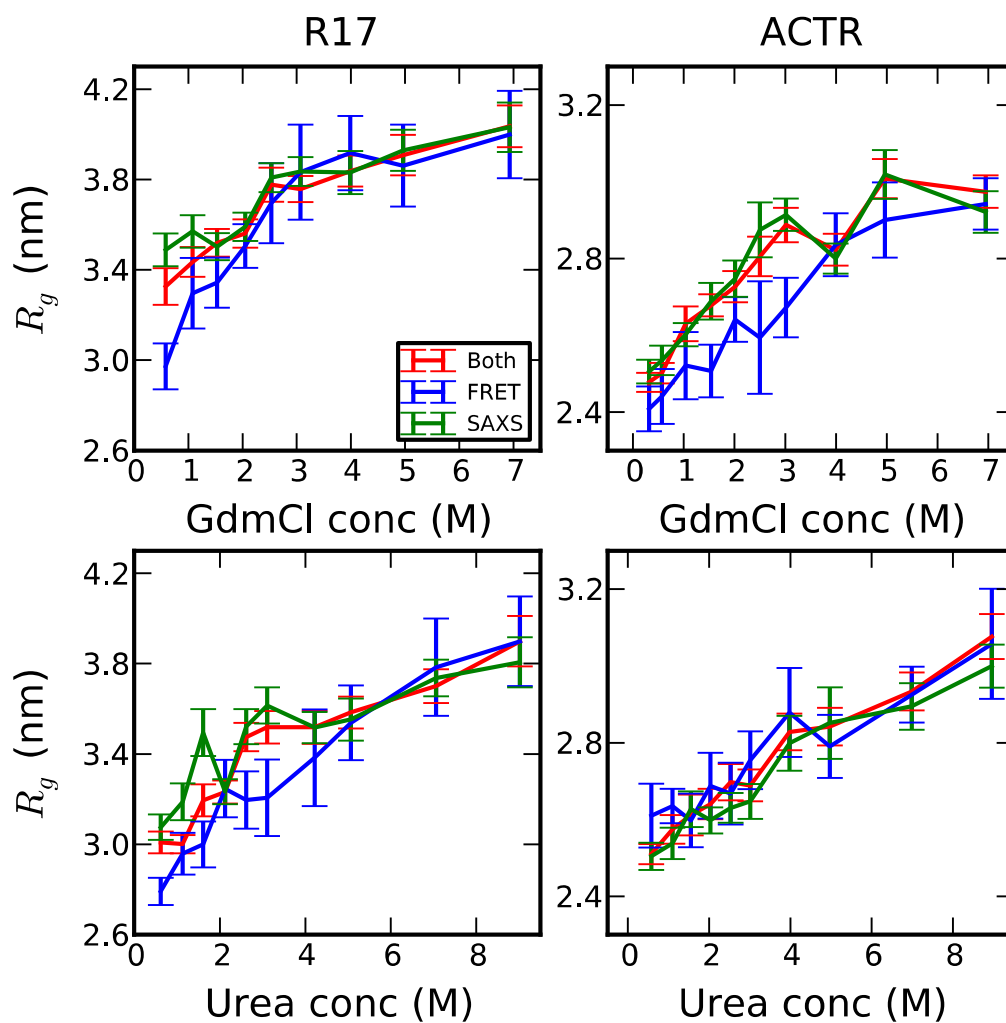


Figure S13. R_g from reweighted ensembles using either only FRET data, only SAXS data, or both SAXS and FRET (see legend for color code).

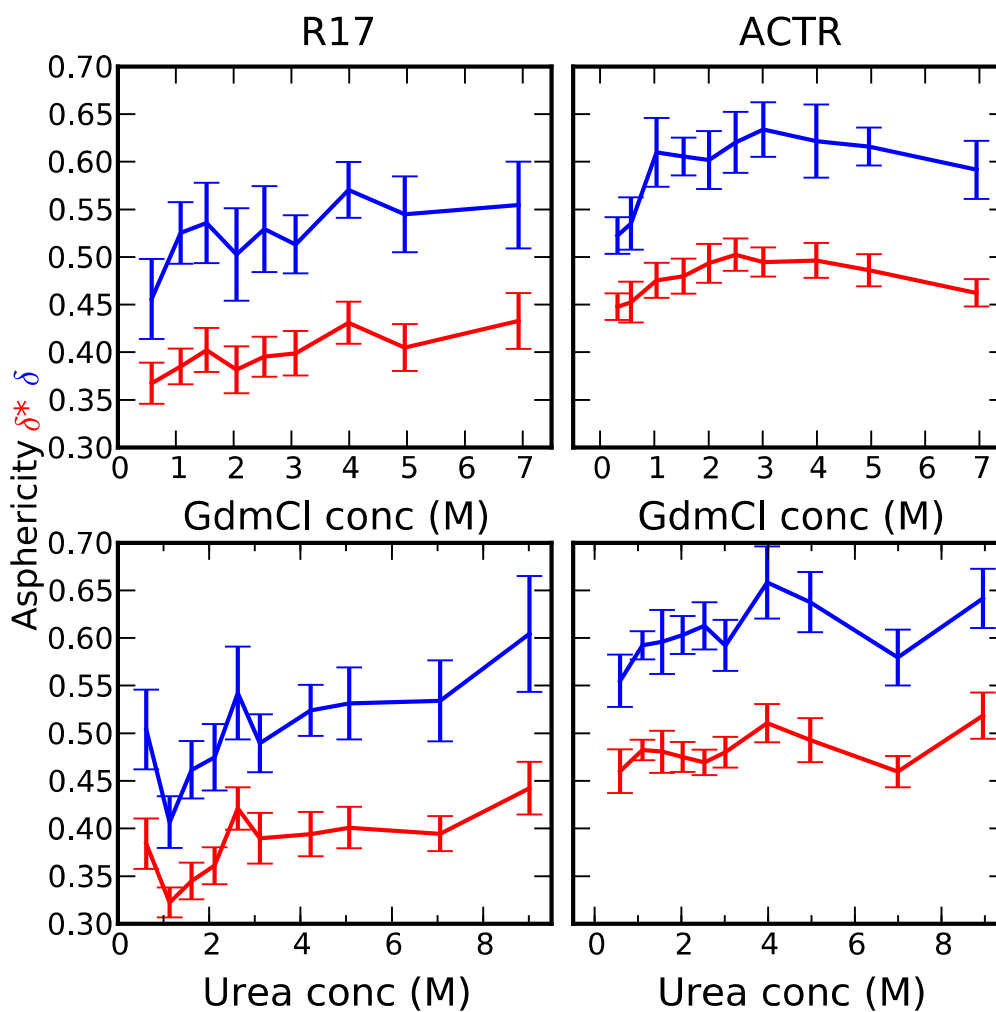


Figure S14. Asphericity of R17d (left) and ACTR (right) in different denaturant concentrations. Asphericity is defined using Eq. 25 and Eq. 26 in reference³⁰, in which δ^* (red) and δ (blue) scale from 0 to 1, with 1 being most aspherical.

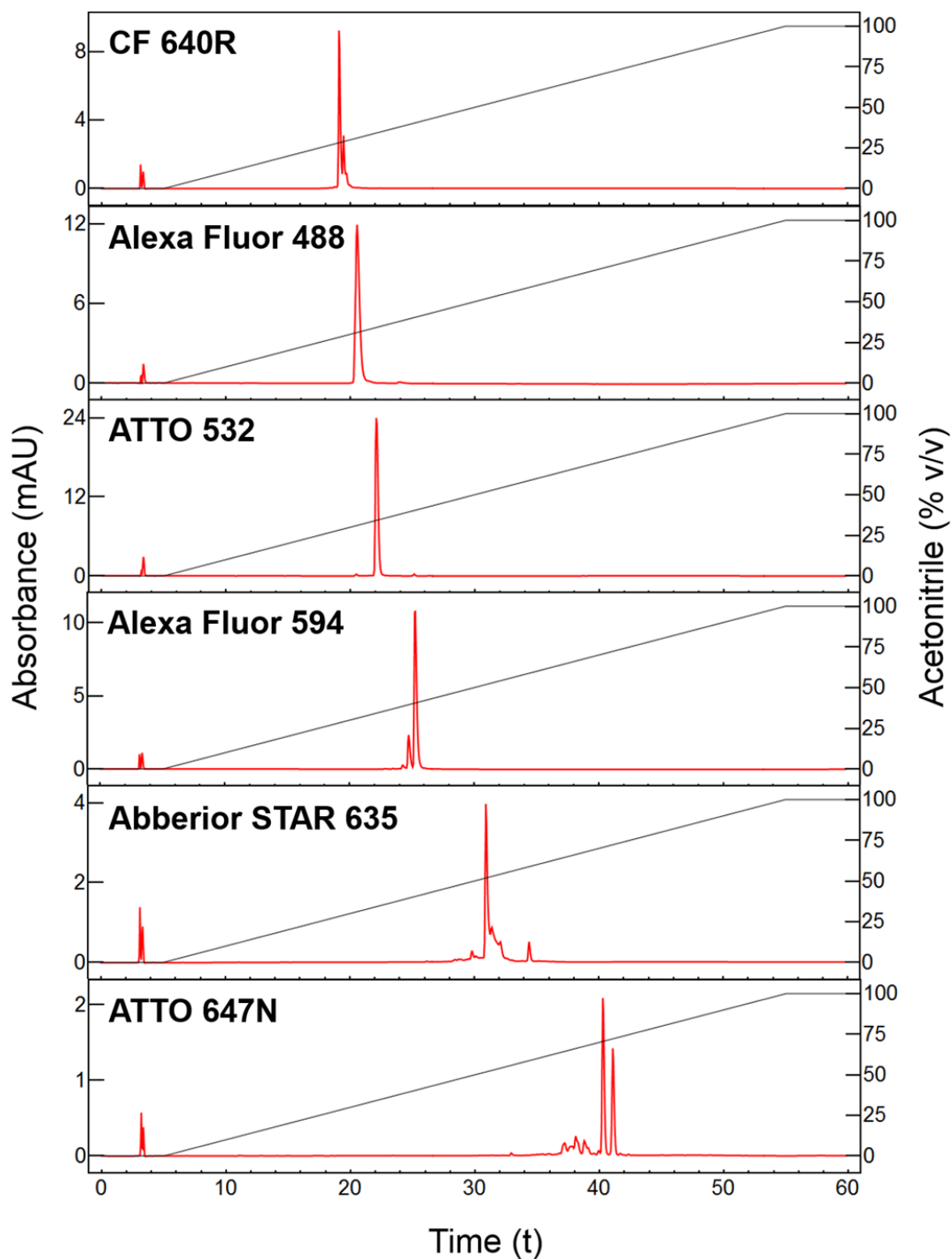


Figure S15. Hydrophobicity of chromophores used for FRET and 2f-FCS. Reversed-Phase-HPLC chromatograms reporting the retention times of different chromophores used for single-molecule spectroscopy; from top to bottom: CF 640R (Biotium), Alexa Fluor 488 (Molecular Probes, Inc), ATTO 532 (ATTO-TEC), Alexa Fluor 594 (Molecular Probes, Inc), ATTO 647N (ATTO-TEC), and Abberior STAR 635 (Abberior). Hydrolyzed dyes were injected on a C18 RP-HPLC column and eluted with a gradient from an aqueous solution containing 0.1% TFA to 100% acetonitrile. Hydrophilic chromophores elute earlier than hydrophobic ones.

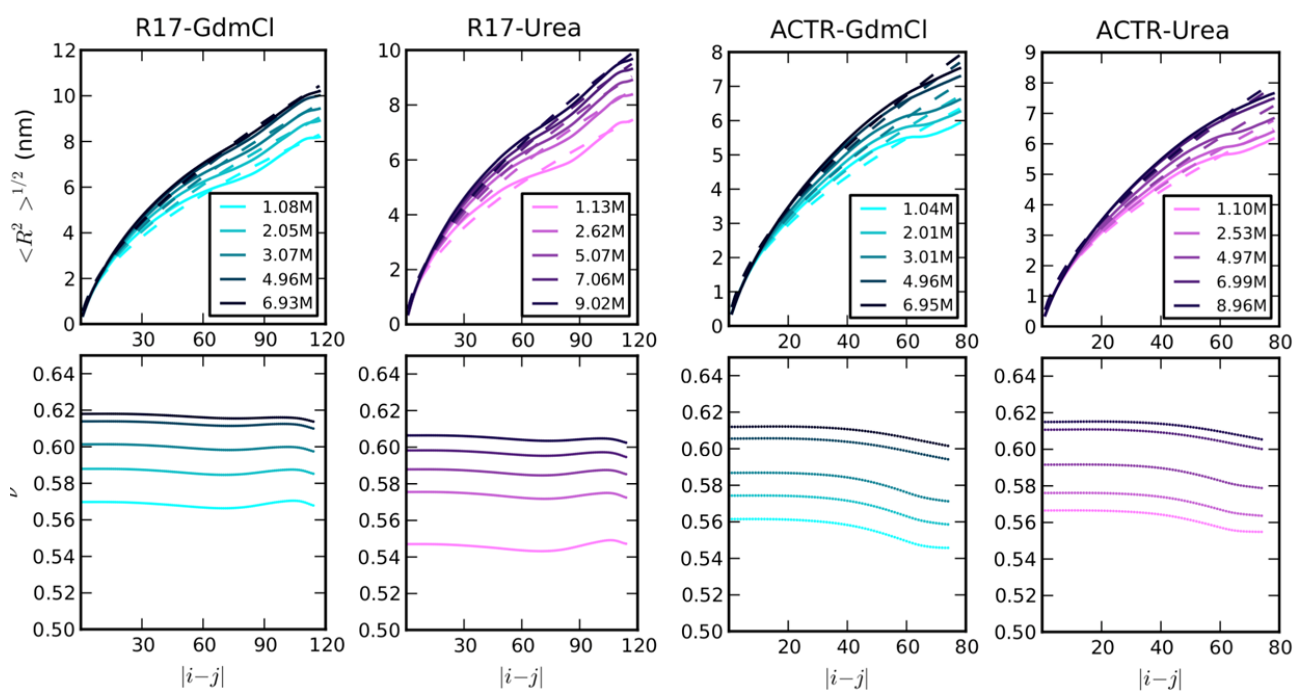


Figure S16. Dependence of inter-residue distance on sequence separation. The top row shows the root-mean-square distance as a function of sequence separation, $|i-j|$, and the bottom row the scaling exponent, ν , resulting from a fit to Eq. S4 with a prefactor of $B = 0.55$.¹⁴ The scaling exponents are plotted in the bottom row as a function of the lowest sequence separation used in the fit (highest is always full chain length).

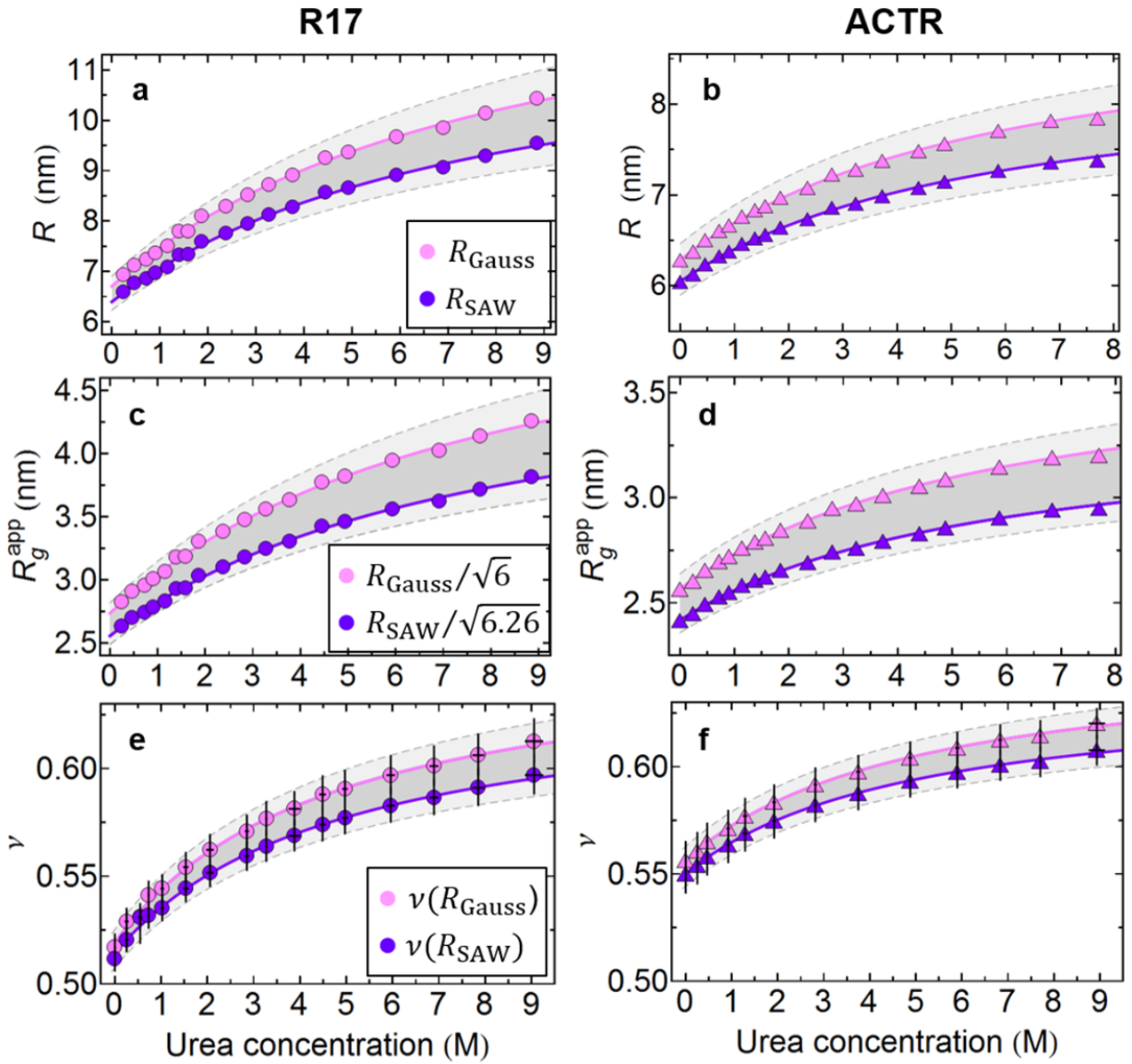


Figure S17. Single-molecule FRET analysis of R17d 1-116 (left column, circles) and ACTR 1-73 (right column triangles) (Table S1) in urea. (a, b) Root-mean-squared values of the end-to-end distance, R , as estimated by assuming the distance distributions of a Gaussian chain (pink) or a self-avoiding walk (SAW, purple). Light shaded areas represent systematic errors propagated from those in transfer efficiency (± 0.02 , see main text and Fig. 2). (c, d) Root-mean-squared radii of gyration (R_g) as inferred from R (a, b) and the expected universal ratios for the Gaussian chain ($R^2/R_g^2 = 6$) or the SAW model ($R^2/R_g^2 \approx 6.26$)¹². (e, f) Scaling exponents obtained by fitting the inter-dye distances of three different protein variants to $R = B|i - j|^\nu$ with a fixed B of 0.55 nm,¹⁴ for both the Gaussian chain and SAW cases. Values and standard deviations from the fits are reported for the inter-dye distances obtained assuming a Gaussian chain (pink) and a SAW model (purple). The fits (solid lines) represent a weak binding model; light shaded areas represent systematic errors propagated from those in transfer efficiency in all cases.

References

- (1) Scott, K. A.; Randles, L. G.; Moran, S. J.; Daggett, V.; Clarke, J. *Journal of Molecular Biology* **2006**, *359*, 159.
- (2) Borgia, A.; Wensley, B. G.; Soranno, A.; Nettels, D.; Borgia, M. B.; Hoffmann, A.; Pfeil, S. H.; Lipman, E. A.; Clarke, J.; Schuler, B. *Nature Comm.* **2012**, *3*, 1195.
- (3) Scott, K. A.; Steward, A.; Fowler, S. B.; Clarke, J. *Journal of Molecular Biology* **2002**, *315*, 819.
- (4) Demarest, S. J.; Martinez-Yamout, M.; Chung, J.; Chen, H.; Xu, W.; Dyson, H. J.; Evans, R. M.; Wright, P. E. *Nature* **2002**, *415*, 549.
- (5) Müller, B. K.; Zaychikov, E.; Bräuchle, C.; Lamb, D. C. *Biophys. J.* **2005**, *89*, 3508.
- (6) Schuler, B. *Methods. Mol. Biol.* **2007**, *350*, 115.
- (7) Nettels, D.; Hoffmann, A.; Schuler, B. *J Phys Chem B* **2008**, *112*, 6137.
- (8) Brucale, M.; Schuler, B.; Samori, B. *Chemical reviews* **2014**, *114*, 3281.
- (9) Kawahara, K.; Tanford, C. *J. Biol. Chem.* **1966**, *241*, 3228.
- (10) Soranno, A.; Buchli, B.; Nettels, D.; Müller-Späth, S.; Cheng, R. R.; Pfeil, S. H.; Hoffmann, A.; Lipman, E. A.; Makarov, D. E.; Schuler, B. *P Natl Acad Sci USA* **2012**, *109*, 17800.
- (11) Nettels, D.; Gopich, I. V.; Hoffmann, A.; Schuler, B. *P Natl Acad Sci USA* **2007**, *104*, 2655.
- (12) Schäfer, L. *Excluded Volume Effects in Polymer Solutions as Explained by the Renormalization Group*; Springer: Berlin, 1999.
- (13) Hoffmann, A.; Kane, A.; Nettels, D.; Hertzog, D. E.; Baumgärtel, P.; Lengefeld, J.; Reichardt, G.; Horsley, D. A.; Seckler, R.; Bakajin, O.; Schuler, B. *P Natl Acad Sci USA* **2007**, *104*, 105.
- (14) Hofmann, H.; Soranno, A.; Borgia, A.; Gast, K.; Nettels, D.; Schuler, B. *Proc. Natl. Acad. Sci. U. S. A.* **2012**, *109*, 16155.
- (15) Scott, K. A.; Batey, S.; Hooton, K. A.; Clarke, J. *J. Mol. Biol.* **2004**, *344*, 195.
- (16) Pace, C. N. *Methods Enzymol.* **1986**, *131*, 266.
- (17) Clarke, J.; Fersht, A. R. *Biochemistry* **1993**, *32*, 4322.
- (18) Provencher, S. W. *Computer Physics Communications* **1982**, *27*, 213.
- (19) Gast, K.; Modler, A. J. In *Protein Folding Handbook*; Buchner, J., Kiefhaber, T., Eds.; Wiley-VCH: Weinheim, 2005; Vol. 2, p 673.
- (20) Vitalis, A.; Pappu, R. V. *J. Comput. Chem.* **2008**, *30*, 673.
- (21) Wuttke, R.; Hofmann, H.; Nettels, D.; Borgia, M. B.; Mittal, J.; Best, R. B.; Schuler, B. *Proc. Natl. Acad. Sci. U. S. A.* **2014**, *111*, 5213.
- (22) Köfinger, J.; Hummer, G. *J Chem Phys* **2015**, *143*, 243150.
- (23) Schwarz, G. *Ann Stat* **1978**, *6*, 461.
- (24) Wensley, B. G.; Batey, S.; Bone, F. A. C.; Chan, Z. M.; Tumelty, N. R.; Steward, A.; Kwa, L. G.; Borgia, A.; Clarke, J. *Nature* **2010**, *463*, 685.
- (25) Batey, S.; Randles, L. G.; Steward, A.; Clarke, J. *Journal of Molecular Biology* **2005**, *349*, 1045.
- (26) Myers, J. K.; Pace, C. N.; Scholtz, J. M. *Protein Science* **1995**, *4*, 2138.
- (27) Pace, C. N. *Methods Enzymol* **1986**, *131*, 266.
- (28) Gopich, I. V.; Szabo, A. *Proceedings of the National Academy of Sciences of the United States of America* **2012**, *109*, 7747.
- (29) Zheng, W.; Borgia, A.; Buholzer, K.; Grishaev, A.; Schuler, B.; Best, R. B. *Submitted* **2016**.
- (30) Steinhauser, M. O. *J Chem Phys* **2005**, *122*.